



ÉCOLE POLYTECHNIQUE FÉDÉRALE DE LAUSANNE

Master Project in Civil Engineering

FRACTURES THERMAL ENERGY STORAGE (FTES)

Conducted in the Geo-energy Laboratory (GEL) at EPFL

Under the supervision of PhD Students Mohsen Talebkeikhah & Tristan Liardon
by

Jean Naftalski

Under the direction of Professor and head of GEL, Brice Lecampion

LAUSANNE, EPFL June 23, 2023

Fractures Thermal Energy Storage (FTES)

This project aims at designing a laboratory-scale experiment to investigate the thermal performance of Fractures Thermal Energy Storage (FTES) systems. While previous field tests have focused on creating horizontal planar fractures at shallow depths, none have explored the circulation of hot fluid through fractures to assess the thermal efficiency of such systems. Similarly, no comprehensive investigation of the heat transfer mechanisms within FTES systems has been conducted at laboratory scale. This work proposes a combined modeling and experimental framework to design a laboratory-scale FTES experiment. The first part of the study introduces analytical and numerical tools to investigate the heat transfer mechanisms occurring at the well and at the fracture. A numerical model is then developed to simulate the entire FTES experiment. In the second part, an initial experimental setup, along with an identification of key operational challenges, are presented. The results obtained from the numerical model and the initial experimental tests highlight the need for improvements in the current experimental setup. Finally, recommendations are provided to address the identified challenges and ensure the successful operation of the FTES experiment.

Keywords: Fractures Thermal Energy Storage, Hydraulic fracturing, Finite Element Heat Transfer Modelling, Experimental Design

Acknowledgements

I would like to express my sincere gratitude to Professor Lecampion for his invaluable guidance and feedback throughout the duration of this project.

I am also deeply thankful to PhD students Tristan Liardon and Mohsen Talebkeikhah for their supervision and support during the experimental part of this project.

Lastly, I am grateful to Dr. Seyyedmaalek Momeni for providing the fracturing data and conducting the fracturing of the gabbro block GB08 prior to the commencement of my project.

Contents

1	Introduction	1
2	Literature Review	4
3	FTES modelling	6
3.1	Governing equations and scalings	6
3.1.1	Fluid flow in fracture	6
3.1.2	Heat transfer in fractured rock	7
3.2	Mathematical modelling	9
3.2.1	Heat transfer around wellbore	9
3.2.2	Heat transfer along fracture	13
3.3	Numerical modelling	15
3.3.1	FEniCS and workflow	15
3.3.2	Time discretization and weak formulation	16
3.3.3	Code validation - Energy balance	18
3.3.4	Heat transfer around wellbore	23
3.3.5	Heat transfer along fracture	24
3.3.6	Modelling of FTES experiment	27
3.4	Discussion	34
4	FTES experiment	36
4.1	Fracture creation	36
4.1.1	Hydraulic fracturing experiment	36
4.1.2	Fracture geometry	38
4.2	Transmissibility tests	39
4.3	Heating system setup	47
4.4	Configuration of fluid temperature at block inlet	48
4.4.1	Non-pressurized injection	48
4.4.2	Pressurized injection	57
4.5	Discussion	58
5	Conclusion	60

List of Figures

1.1	Principle outline of a FTES system (from Larson (1984))	2
1.2	Characterization of gabbro block GB08	3
3.1	Schematic representation of wellbore heat transfer problem (from Ramey Jr (1962))	10
3.2	Workflow for mesh generation with Gmsh	16
3.3	Cross-section geometry of the 3D mesh used for code validation	19
3.4	3D mesh used for code validation	20
3.5	Evolution of the different energy components with time	21
3.6	Comparison of energy given to the system vs energy stored within the system over time	22
3.7	Comparison of analytical and numerical solutions for wellbore fluid temperature at different times (water flow rate $Q = 2$ mL/min)	23
3.8	3D mesh used for modelling of heat transfer along the fracture	25
3.9	Comparison of analytical and numerical solutions for fracture fluid temperature at different times (water flow rate $Q = 20$ mL/min)	26
3.10	Structured meshes generated for the resolution of the flow and heat transfer problems	28
3.11	Influence of the interpolation order for the fluid pressure field on the solution of the heat transfer problem (utilizing order 1 interpolation for the temperature field) . .	30
3.12	Influence of the interpolation order for the temperature field on the solution of the heat transfer problem (utilizing order 3 interpolation for the fluid pressure field) . .	31
3.13	Influence of fluid flow rate on the charging rate of the FTES system	32
3.14	Evolution of the temperature along the well with time	32
3.15	Evolution of the temperature along the fracture with time	33
3.16	Evolution of the temperature at point A with coordinates (0.125, 0, 0.188) over time	34
4.1	Hydraulic fracturing of gabbro block GB08	37
4.2	Visualization of fracture front propagation using acoustic emission data. The plot was generated by Dr. Seyyedmaalek Momeni, who performed the fracturing of the block.	38
4.3	Estimation of fracture geometry through fracture trace data	39
4.4	Experimental setup for fracture transmissibility estimation	41
4.5	Observation of elastohydrodynamic effects when flow rate stages are imposed by the pump	42
4.6	Evolution of pressure, flow rate and injected water volume with time	43
4.7	Impact of data aggregation group size on water flow rate data visualization	44
4.8	Evolution of fracture transmissibility with pressure	45

4.9	Geometry of the initial fracture extension and trace of the newly created fracture .	46
4.10	Comparison of transmissibility between the initial fracture, the initial fracture with the opened new fracture, and the initial fracture with the clogged new fracture . . .	46
4.11	Experimental setup for heating system	48
4.12	Initial FTES experiment setup	49
4.13	Experimental setup for water temperature measurement at the connector	49
4.14	Evolution of water temperature at the connector for various flow rates (silicone oil temperature $T_{oil} = 130^{\circ}\text{C}$)	50
4.15	Schematic representation of the tubing cross section and corresponding physical properties	51
4.16	Fluid temperature profile along the tubing for various flow rates	54
4.17	Modification of the FTES experimental setup: tubing isolation and shortening . . .	55
4.18	Tubing insulation process and result	56
4.19	Evolution of water temperature at the connector for various flow rates (new experimental setup)	56
4.20	Photograph of the insulated gabbro block GB08	57

List of Tables

3.1	Material parameters of the numerical model	19
3.2	Values of the geometrical dimensions illustrated in Figure 3.3a	20
3.3	Geometrical dimensions of the FTES experiment numerical model	29

1 Introduction

One of the major challenges in contemporary energy production is the ability to store the surplus of energy generated during periods of low demand compared to supply. This challenge is exacerbated by the intermittent nature of certain renewable energy sources, such as wind and solar power, whose production is subject to significant variability depending on meteorological and other environmental conditions. Thermal energy storage is one potential solution for addressing this issue. Several technologies have been developed to store energy in the form of sensible heat (without phase change): BTES (Borehole Thermal Energy Storage), ATES (Aquifer Thermal Energy Storage), CTES (Cavern Thermal Energy Storage), etc.

The concept of Fractures Thermal Energy Storage (FTES) follows two main observations regarding thermal energy storage. The first is that many of the existing thermal energy storage technologies require a particular geological context. For example, ATES is a very efficient system for seasonal energy storage, as it is economical and has a large storage volume. However, it requires the presence of an aquifer that fulfils certain geo-hydrological constraints: the aquifer must be sufficiently large, and the hydraulic gradient must be low to minimise advective heat loss (Bloemendal et al., 2015). The second observation addresses the financial feasibility of the project. Indeed, most thermal energy storage technologies (TES) require a relatively large initial investment. This is the case for BTES, which consists of a grid of borehole heat exchangers (BHEs) inserted in the rock mass (Janiszewski, 2019). In contrast to these technologies, Fractures Thermal Energy Storage (FTES) does not require specific geological conditions and could be implemented in both low permeability rocks and soils. Moreover, the construction cost of the storage system is reduced by almost 50% compared to conventional BTES systems, as the number of boreholes to drill is minimized (Ramstad et al., 2007).

Fractures Thermal Energy Storage (FTES) systems are built by hydraulically fracturing in vertical boreholes to create multiple parallel fracture planes within the rock. At shallow depth, as the horizontal stress is greater than the vertical stress (reverse faulting stress regime), these fractures will propagate almost horizontally through the rock (Larson, 1984). During the hydraulic fracturing process, the fractures are kept open by injecting proppants (often sand or ceramic balls). FTES systems behave like large heat exchangers, where water is the heat carrier fluid and rock is the storage medium (Larson, 1984). In such systems, the energy is transferred by convection in the fractures and then by conduction into the rock. Finally, FTES systems can serve two purposes: cooling water in summer by introducing warm water through the discharged system (which matches the temperature of the surrounding area), and heating water in winter by introducing cold water through the charged system (which has a higher temperature than the surrounding area) (Larson,

1984).

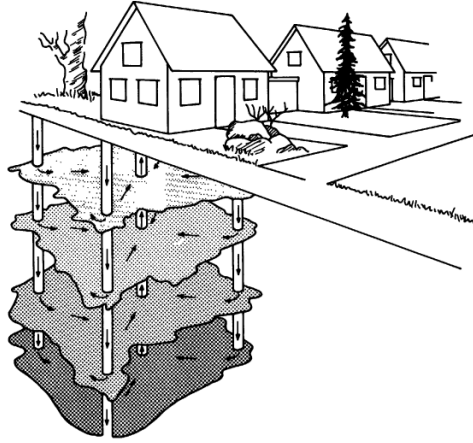
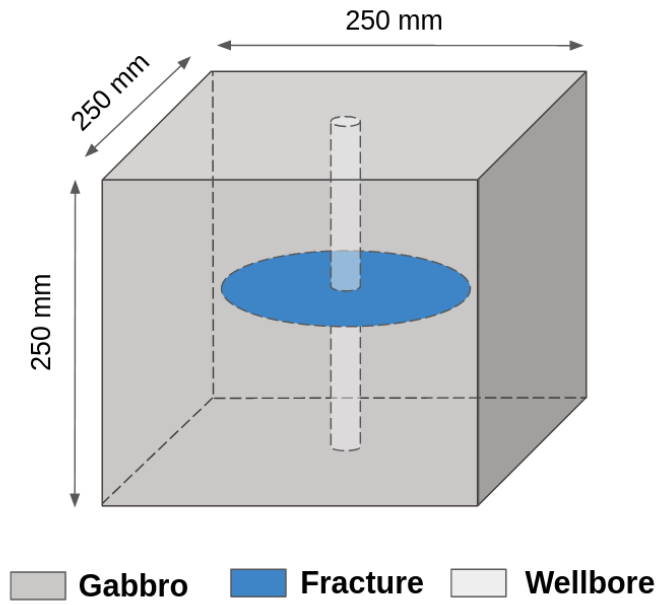


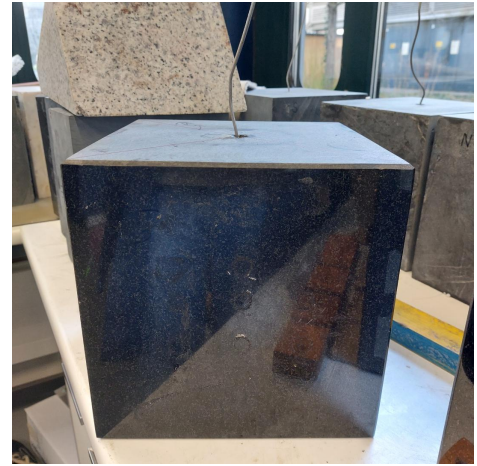
Figure 1.1: Principle outline of a FTES system (from Larson (1984))

The objective of this project is to design a laboratory-scale FTES experiment to conduct a comprehensive investigation into the thermal performance of such system. For this purpose, the experiment was first numerically modelled, and simplified analytical solutions were presented to investigate the heat transfer mechanisms occurring at the well and at the fracture. Then, a preliminary setup was developed and tested for the laboratory experiment.

To conduct the laboratory-scale FTES experiment, a cubic sample of Zimbabwe gabbro with a side length of 250mm was chosen. The very low permeability of gabbro provides significant benefits in the successful development of an FTES system, as it ensures that the fluid flows exclusively through the fractures. Before the initiation of the project, a vertical wellbore with a diameter of 17mm was drilled through the entire height of the block. A horizontal radial notch was then created by rotating a T-shaped notching tool (Liu and Lecampion, 2022). Finally, a completion tool connected to an injection tubing was glued in the wellbore using epoxy resin to ensure that the fluid is only injected at the level of the notch. Subsequently, the cube was hydraulically fractured by injecting water at a constant flow rate from the central wellbore. The details of the specimen fracturing are provided in Section 4.1.1, and a simplified schematic illustration of the block is shown in Figure 1.2a.



(a) Schematic geometry of GB08



(b) Photograph of GB08

Figure 1.2: Characterization of gabbro block GB08

2 Literature Review

The Fractures Thermal Energy Storage (FTES) method derives from the HYDROCK concept, which was originally formulated and developed in Sweden during the early 1980s (Larson et al., 1983; Larson, 1984). The aim of the HYDROCK concept was to store thermal energy in a shallow hard rock aquifer that has been artificially fractured by means of hydraulic fracturing. Most of the project's research focused on the design and the hydraulic aspect of the system operation. For instance, Larson (1984) conducted a field experiment at Rixö (Sweden) to investigate the creation of subhorizontal parallel stacked fractures at shallow depth within the Bohus granite. The research results suggested that while the creation of such fractures through hydraulic fracturing is technically feasible, it is recommended to introduce proppants within the fractures to reduce the impedance within the system and to achieve efficient flow control (Larson, 1984). Other contemporary studies, notably those conducted at Fjällbacka (Sweden) in the framework of the Hot Dry Rock (HDR) project, have confirmed the importance of incorporating proppants to keep the fractures open and to reduce the near-well pressure losses in the circulation phase (Sundquist et al., 1988; Eliasson et al., 1988).

In the late 1990s, a research project was initiated in Norway with the aim of exploring various hydraulic fracturing techniques that could enhance energy extraction through the creation of larger heat exchange areas within the bedrock (Ramstad, 2004). A comprehensive hydraulic stimulation program was conducted at two pilot plants located in the municipality of Bærum near Oslo (Norway), whose configuration is quite similar to that of the HYDROCK concept. The results of pumping tests and geophysical logging indicated that the use of sand as a propping agent is essential in fractures with high counter pressures (>40 bars), and that the particle size of the sand should be adjusted according to the counter pressure (Ramstad et al., 2007).

Although none of the previously mentioned field tests have involved hot water circulation, a few numerical models have been developed to better understand the heat transfer occurring within FTES systems. For instance, Hellström and Larson (2001) used the explicit Finite Difference Method (FDM) to simulate the coupled conductive-convective heat transfer process occurring in a HYDROCK store. Their findings revealed that the heat transfer capacity of a HYDROCK store depends mainly on geometrical parameters such as the spacing of the cracks and the distance between the central well and peripheral wells, as well as on the water flow rate. Similarly, Ramstad (2004) modeled the Bryn and EAB pilot plants using the finite element software FEFLOW (Finite Element subsurface FLOW system). Their study emphasizes the importance of heat exchange area and thermal conductivity of the bedrock for determining the energy potential of the system.

More recently, Hesselbrandt and Acuna (2022) proposed a numerical approach for modeling FTES systems also based on the finite element code FEFLOW, which allows for relatively simple and computationally efficient simulation of the intricate hydraulic and thermal processes involved in a FTES system.

Despite the increasing interest in FTES systems, large-scale field applications of this technology has not been tested yet (Janiszewski, 2019), and no laboratory-scale experiment have been reported in the literature to date. The objective of the present work is thus to set up a laboratory-scale experiment to investigate the thermal behavior of FTES systems under controlled conditions, and to gain insights into the key design and operational parameters affecting their performance. In parallel with this work, a 10-meter-scale field test will soon begin at the Sanford Underground Research Facility (SURF). This test will involve the utilization of five pre-existing drilled wells to conduct hot water circulation tests between the central well and the four surrounding wells.

3 FTES modelling

3.1 Governing equations and scalings

3.1.1 Fluid flow in fracture

In a FTES system, the key element that allows the transfer of energy to the host rock is the heat transfer fluid. There are many types of heat transfer fluids, but the most commonly used is water because of its low cost and favourable physical properties (high heat capacity and low viscosity). The amount of heat exchanged with the rock depends not only on the exact nature of this fluid but also on the fluid flow pattern within the fractures. This pattern, which is inherently linked to the fracture geometry, can be determined by jointly solving the Navier-Stokes and the continuity equation:

$$\mu \nabla^2 u - \rho (\nabla u) u = \nabla p \quad (1)$$

$$\nabla \cdot u = 0 \quad (2)$$

where ρ and μ are respectively the density and the dynamic viscosity of the fluid, u is the velocity vector and p is the fluid pressure. It should be noted that the transient term in the Navier-Stokes equation was omitted as fracture permeability is generally defined for steady-state flow. Additionally, the continuity equation, which represents the conservation of mass, was formulated under the assumption of an incompressible fluid.

Analytically, the Navier-Stokes equation can be solved in the simple configuration where the fracture is modelled by two smooth and parallel plates separated by a constant aperture h . For a uniform pressure gradient within the fracture plane, the total volumetric flux Q through the fracture is given by the Cubic Law (Zimmerman and Bodvarsson, 1996):

$$Q = -\frac{\rho g h^3 W}{12\mu} \frac{\Delta H}{L} \quad (3)$$

where g is the gravitational acceleration, h is the fracture aperture, W and L are respectively the width and the length of the fracture, and H is the hydraulic head. By comparing this expression with Darcy's law in one dimension, the permeability of the fracture can be defined as:

$$k = \frac{h^2}{12} \quad (4)$$

In general, it is more convenient to work directly with the transmissibility of the fracture, which is defined as the product of the permeability with the thickness of the fracture:

$$T = kh = \frac{h^3}{12} \quad (5)$$

For more complex fracture geometries and boundary conditions, the distribution of pressure and flow within the fracture can be determined by solving the Reynolds equation numerically:

$$\nabla \cdot \left(\frac{h^3(x, y)}{12\mu} \nabla p \right) = 0 \quad (6)$$

This expression is derived straightforwardly from Equation 2, assuming a local cubic law for the flow, and results in a parabolic partial differential equation (PDE).

However, the applicability of the Reynolds equation is limited to situations where the Reynolds number, representing the balance between inertial and viscous forces within the fluid, remains low, and when the aperture of the fracture does not vary too abruptly (Zimmerman and Bodvarsson, 1996). Furthermore, in real rock fractures, the Reynolds equation has been found to overestimate the flow by up to 100% compared to the actual flow (Yeo and Ge, 2005). For high Reynolds numbers or if the fracture aperture varies significantly within the fracture, it is thus more appropriate to solve numerically Equations 1 and 2 (Chen et al., 2014).

3.1.2 Heat transfer in fractured rock

The heat transport within a fractured rock medium is governed by the diffusion-advection equation, which derives from the principle of energy conservation. In the following explanations, two main assumptions are made. Firstly, it is assumed that the rock is impermeable, and therefore, the flow occurs exclusively through fractures. Secondly, the fractures are assumed to be unpropped, meaning their permeability arises solely from their opening. The heat transfer within a propped fracture can be derived straightforwardly by considering an equivalent porous medium and assuming a local thermal equilibrium between the fluid phase and the solid matrix. With these two assumptions, the heat transfer mechanism within the FTES system can be decomposed into two parts:

- Within a fracture, there is both heat advection due to the fluid motion and heat diffusion within the fluid itself. Consequently, the local energy conservation within a representative volume element (RVE) of fluid, assuming no phase change, can be expressed as follows:

$$\rho_w c_w \frac{\partial T}{\partial t} + \nabla \cdot (\mathbf{Q}_{\text{adv}} + \mathbf{Q}_{\text{diff}}) = \rho_w c_w \gamma \quad (7)$$

where ρ_w, c_w are respectively the density and the heat capacity of water, and γ is a source

term. The advective flux \mathbf{Q}_{adv} is given by:

$$\mathbf{Q}_{\text{adv}} = \rho_w c_w \mathbf{q} T \quad (8)$$

where \mathbf{q} is the fluid velocity vector. On the other hand, the diffusive flux \mathbf{Q}_{diff} (i.e. heat conduction process) is given by Fourier's law:

$$\mathbf{Q}_{\text{diff}} = -\lambda_w \nabla T \quad (9)$$

where λ_w is the thermal conductivity of water.

- In the rock, since it is considered impermeable, heat transport only occurs through conduction, and the local energy conservation within a rock RVE can be expressed as follows:

$$\rho_r c_r \frac{\partial T}{\partial t} + \nabla \cdot \mathbf{Q}_{\text{diff}} = \rho_r c_r \gamma \quad (10)$$

where ρ_r, c_r are respectively the density and the heat capacity of the rock. Note that this time, in the expression of the diffusive flux, the thermal conductivity of the rock λ_r should be chosen.

Assuming that the fluid is incompressible (i.e. $\nabla \cdot \mathbf{q} = 0$), Equation 7 can be rewritten as:

$$\frac{\partial T}{\partial t} + \mathbf{q} \cdot \nabla T - \nabla \cdot (\alpha_w \nabla T) = \gamma \quad (11)$$

where α_w is the thermal diffusivity of water which is defined as $\alpha_w = \frac{\lambda_w}{\rho_w c_w}$. The resulting equation is a combination of a parabolic and a hyperbolic PDE. The parabolic term describes a heat diffusion phenomenon within the fluid, while the hyperbolic term describes an advective heat transfer phenomenon. Furthermore, when the source term is neglected, this equation can be effectively rewritten into the subsequent dimensionless forms:

1. If a characteristic diffusive time scale $t^* = \frac{(L^*)^2}{\alpha_w}$ is chosen:

$$\frac{\partial \Theta}{\partial \tau} = \nabla^2 \Theta - \text{Pe} \boldsymbol{\Upsilon} \cdot \nabla \Theta \quad (12)$$

2. If a characteristic advective time scale $t^* = \frac{L^*}{Q^*}$ is chosen:

$$\frac{\partial \Theta}{\partial \tau} = \frac{1}{\text{Pe}} \nabla^2 \Theta - \boldsymbol{\Upsilon} \cdot \nabla \Theta \quad (13)$$

In both of the previous dimensionless equations, Pe is the Péclet number defined as $\text{Pe} = \frac{L^* Q^*}{\alpha_w}$, and L^* and Q^* are respectively a characteristic length scale and a characteristic fluid velocity of the

problem. On the other hand, Θ , τ , and Υ are respectively the dimensionless temperature, time, and fluid velocity defined as follows:

$$\Theta = \frac{T - T_0}{T^*} \quad , \quad \tau = \frac{t}{t^*} \quad , \quad \Upsilon = \frac{\mathbf{q}}{Q^*} \quad (14)$$

with T^* a characteristic temperature of the problem.

The Péclet number is useful for studying heat or mass transport phenomena in a continuum, as it quantifies the ratio of convective to diffusive heat or mass transfer.

Similarly to Equation 7, Equation 10 can be rewritten in a dimensionless form. As the equation describes a heat conduction process within the rock, the characteristic time scale is chosen to be $t^* = \frac{(L^*)^2}{\alpha_r}$, and Equation 10 becomes:

$$\frac{\partial \Theta}{\partial \tau} = \nabla^2 \Theta \quad (15)$$

where α_r is the thermal diffusivity of the rock, and L^* is a characteristic length scale of the problem.

3.2 Mathematical modelling

This section addresses a number of mathematical models that are necessary for the general understanding of a FTES system. The objective is to separately study the heat transfer that occurs along the well from the heat transfer that occurs along the fractures.

3.2.1 Heat transfer around wellbore

The fluid injection flow rate into the well emerges as a crucial parameter in the design of a FTES system. Indeed, heat losses along the injection well can be significant depending on the rock properties and the fluid velocity within the well. Therefore, it is imperative to ensure that not all of the heat is lost along the well, and that the temperature of the water infiltrating the fractures remains sufficiently high.

The majority of existing literature on wellbore heat transfer relies on the work of Ramey Jr (1962), who developed a method to calculate the temperature in injection and production wells. His work, along with most of the subsequent research, is based on the following assumptions:

1. Fluid flows in a straight, one-dimensional well. Therefore, the temperature of the wellbore fluid depends only on depth and time.
2. Conductive heat flux occurs only in the radial direction.
3. Physical and thermal properties of the earth and wellbore fluid do not vary with temperature.

4. The accumulation term is negligibly small in the wellbore fluid heat balance.
5. Heat transmission in the wellbore is rapid compared to heat flow in the formation.

In his work, Ramey Jr (1962) further assumes a vanishingly small wellbore radius to derive the temperature distribution around the well (line source model). Instead, in this section, we adopt the model proposed by Hasan and Kabir (1991) as it assumes a cylindrical heat source model, which is more accurate for early-time borehole temperature predictions.

Consider the problem illustrated in Figure 3.1, where the tubing has an inner radius R_1 , and the temperature T_1 of the fluid inside the tubing varies with both depth Z and time t . On the other hand, the casing outer radius is R_2 and its surface is at temperature T_2 , which can also vary with depth and time.

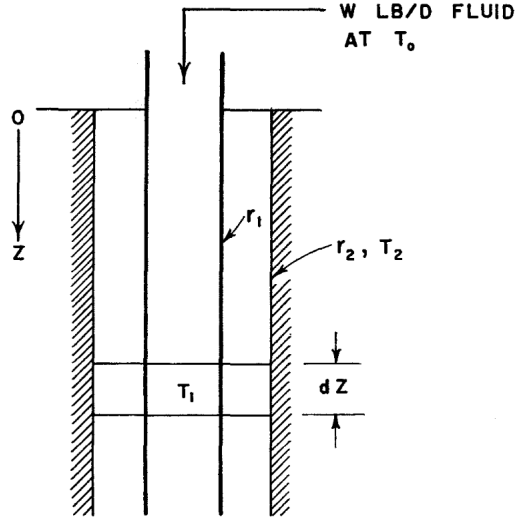


Figure 3.1: Schematic representation of wellbore heat transfer problem (from Ramey Jr (1962))

Based on Equation 7, the heat balance within the tubing reads:

$$\rho_w c_w \frac{\partial T_1}{\partial t} + c_w \rho_w u \frac{\partial T_1}{\partial z} = - \frac{q(T_1, z, t)}{\pi R_1^2} \quad (16)$$

where u is the fluid velocity and q is the radial conductive heat-loss rate from the fluid to the tubing which is given by:

$$q = 2\pi R_1 \lambda_{tubing} \left(\frac{\partial T_1}{\partial r} \right) \Big|_{r=R_1} \quad (17)$$

According to Hypothesis 4, the accumulation term is negligibly small in the wellbore fluid heat balance:

$$\rho_w c_w \frac{\partial T_1}{\partial t} = 0 \quad (18)$$

This hypothesis is not valid at early stages when the hot inlet fluid replaces the initial tubing fluid because in this period, the temperature profile in the tubing is coupled to the displacement front controlled by the accumulation term (Hagoort, 2004). However, after a certain point, the accumulation term may become negligibly small as the tubing temperature change progressively diminishes with time (Hagoort, 2004).

Furthermore, Hypothesis 5 states that heat transmission in wellbore components (tubing, cement, casing, etc.) is rapid compared to heat flow in the formation. Therefore, the heat transfer through the wellbore components could be rewritten in the following form:

$$q = 2\pi R_1 U (T_1 - T_2) \quad (19)$$

where U is a constant overall heat transfer coefficient which depends on the thermal resistance of each wellbore component. For example, if the wellbore consists only of a cemented tubing and if the resistance of the water film inside the tubing is negligible, the overall heat transfer coefficient reads:

$$\frac{1}{U} = \frac{r_{t0} \ln(r_{t0}/r_{ti})}{\lambda_t} + \frac{r_{t0} \ln(r_{c0}/r_{ci})}{\lambda_c} \quad (20)$$

where r_{ti} and r_{t0} represent the inner and outer radii of the tubing, respectively, and r_{ci} , r_{c0} denote the inner and outer radii of the cement layer. The first term of the sum accounts for the thermal resistance of the tubing, while the second term accounts for that of the cement.

Finally, the heat balance in the tubing (Equation 16) becomes:

$$W c_w \frac{\partial T_1}{\partial z} = -2\pi R_1 U (T_1 - T_2) \quad (21)$$

where W is the total mass flow rate ($W = \pi R_1^2 \rho_w u$).

In a similar way, the heat balance in the formation (pure diffusion in cylindrical coordinates) can be written as:

$$\frac{c_e \rho_e}{\lambda_e} \frac{\partial T_e}{\partial t} = \frac{\partial^2 T_e}{\partial r^2} + \frac{1}{r} \frac{\partial T_e}{\partial r} \quad (22)$$

where T_e is the earth temperature, r is the radial distance from the center of the well, and $\lambda_e/(\rho_e c_e)$ is the formation thermal diffusivity.

At the initial state, the formation is at a constant temperature T_{ei} . At the outer boundary or at infinity, the heat flux is zero. Finally, at the interface of the wellbore with the formation, the heat

flux is determined from Equation 21:

$$\left(\frac{\partial T_e}{\partial r}\right)\bigg|_{r=R_2} = \left(\frac{\partial T_2}{\partial r}\right)\bigg|_{r=R_2} = -\frac{W c_w}{2\pi R_2 \lambda_e} \frac{\partial T_1}{\partial z} \quad (23)$$

In their work, Hasan and Kabir (1991) introduce the dimensionless variables r_D (dimensionless radial distance = r/R_2), α_e (thermal diffusivity = $\lambda_e/(\rho_e c_e)$), and t_D (dimensionless diffusive time = $\alpha_e t/R_2^2$), which allows for the following rewriting of equations 22 and 23:

$$\frac{\partial T_e}{\partial t_D} = \frac{\partial^2 T_e}{\partial r_D^2} + \frac{1}{r_D} \frac{\partial T_e}{\partial r_D} \quad (24)$$

$$\left(\frac{\partial T_e}{\partial r_D}\right)\bigg|_{r_D=1} = -\frac{W c_w}{2\pi \lambda_e} \frac{\partial T_1}{\partial z} \quad (25)$$

By examining Equation 25, it is clear that this Neumann condition is not constant since the term $\partial T_1/\partial z$ depends on time. Assuming, for the moment, that this ratio is constant, Equation 24 can be solved using Laplace transform, and the solution evaluated at the wellbore ($R_D = 1$) reads (Hasan and Kabir, 1991):

$$T_2 = T_{ei} + \frac{c_w W}{\pi^2 \lambda_e} \frac{\partial T_1}{\partial z} I \quad (26)$$

where

$$I = \int_0^\infty \frac{1 - e^{-u^2 t_D}}{u^2} \frac{Y_1(u)J_0(u) - J_1(u)Y_0(u)}{J_1^2(u) + Y_1^2(u)} du \quad (27)$$

J_0 and J_1 represent the zero and first-order Bessel functions of the first kind, while Y_0 and Y_1 denote the zero and first-order modified Bessel functions of the first kind, respectively. T_{ei} is the initial formation temperature.

There exist multiple approaches for solving linear differential equations with time-dependent boundary conditions (non-homogeneous equations). For example, in structural engineering, it is common to use Duhamel's convolution theorem to analyze the response of structures to time-varying loads. In their study, Hasan and Kabir (1991) propose to use the principle of superposition by discretizing time into multiple steps, during which they assumed that the heat flow remains constant:

$$T_2 = T_{ei} + \frac{c_w}{\pi^2 \lambda_e} \sum_{j=1}^n \left[W \frac{\partial T_1}{\partial z} \right]_j \Delta I \quad (28)$$

where

$$\Delta I = \int_0^\infty \frac{1 - e^{-u^2 \Delta t_D}}{u^2} \frac{Y_1(u)J_0(u) - J_1(u)Y_0(u)}{J_1^2(u) + Y_1^2(u)} du \quad (29)$$

However, this approach requires knowledge of the history of heat transfer rate from the wellbore to

the formation (terms in Equation 28 summation), which is part of the problem's solution. Thus, the problem is nonlinear and difficult to solve analytically without resorting to numerical methods. Consequently, nearly all models developed to determine wellbore fluid temperature rely on the assumption of a constant heat flux between the wellbore fluid and the formation, which means that the effect of temperature history on heat loss is ignored. This condition can be approached after some time when both heat loss and temperature vary slowly with time (Hagoort, 2004).

Based on the assumption of a constant heat flux between the fluid and the formation, Hasan and Kabir (1991) introduced a dimensionless temperature T_D , which is defined as:

$$T_D = -\frac{2\pi\lambda_e}{c_w} \frac{T_2 - T_{ei}}{W(\partial T_1 / \partial z)} = -\frac{2I}{\pi} \quad (30)$$

They also provide an approximate solution of T_D to avoid time-consuming computations of the I integral:

$$T_D = 1.1281\sqrt{t_D}[1 - 0.3\sqrt{t_D}] \quad \text{if } t_D \leq 1.5 \quad (31)$$

$$T_D = [0.4063 + 0.5 \ln t_D] \left[1 + \frac{0.6}{t_D} \right] \quad \text{if } t_D > 1.5 \quad (32)$$

In summary, two equations are available for calculating the temperature gradient within the wellbore fluid:

$$\frac{dT_1}{dz} = -\frac{2\pi R_1 U}{c_w W} (T_1 - T_2) \quad (33)$$

$$\frac{dT_1}{dz} = -\frac{2\pi\lambda_e}{c_w W T_D} (T_2 - T_{ei}) \quad (34)$$

By combining the two equations, the unknown T_2 is eliminated, resulting in a first-order ODE with only T_1 as the unknown:

$$\frac{dT_1}{dz} = -\frac{2\pi}{c_w W} \left[\frac{R_1 U \lambda_e}{\lambda_e + R_1 T_D U} \right] (T_1 - T_{ei}) \quad (35)$$

The result of this equation is:

$$T_1(z, t) = T_{ei} + e^{-Az} (T_{1,wh} - T_{ei}) \quad (36)$$

where $T_{1,wh}$ is the fluid temperature at the wellhead, and:

$$A = \frac{2\pi}{c_w W} \left[\frac{R_1 U \lambda_e}{\lambda_e + R_1 T_D U} \right] \quad (37)$$

3.2.2 Heat transfer along fracture

What makes the specificity of an FTES system is that the majority of heat transfer does not occur from the well, as in BTES systems, but from the fractures. It is therefore essential to understand

how heat transfer occurs from the fractures to the rock. As explained in Section 3.1.1, flow within a fracture can be complex, depending on the fracture's geometry and boundary conditions. Therefore, in this section, we assume a steady radial flow from the well through the fracture.

To the best of the author's knowledge, no prior studies have formulated mathematical models to investigate the temperature profile of fluid flowing radially within a 2D planar fracture embedded in a 3D formation. The developments that follow are based on the following assumptions:

1. The fluid flows radially from the center of the fracture, where a total fluid mass flow rate W is injected through a well.
2. The conductive heat flux only occurs perpendicular to the plane of the fracture (in the z direction).
3. Physical and thermal properties of the earth and fracture fluid do not vary with temperature.
4. The accumulation term is negligibly small in the fracture fluid heat balance.

Based on Equation 7 and Hypothesis 4, the heat balance within the fracture reads:

$$c_w W \frac{\partial T_f}{\partial r} = -q(T_f, r, t) \quad (38)$$

where

$$q = 2 \cdot 2\pi r \lambda_e \left(\frac{\partial T_f}{\partial z} \right) \Big|_{z=0} \quad (39)$$

The first factor 2 accounts for the fact that there is 1D diffusion both upwards and downwards from the fracture.

On the other hand, the heat balance in the formation can be written (pure 1D diffusion):

$$\frac{\partial T_e}{\partial t} = \alpha_e \frac{\partial^2 T_e}{\partial z^2} \quad (40)$$

with the following boundary condition derived from Equation 38:

$$\left(\frac{\partial T_e}{\partial z} \right) \Big|_{z=0} = -\frac{W c_w}{4\pi r \lambda_e} \frac{\partial T_f}{\partial r} \quad (41)$$

Assuming, as in previous section, that the $\partial T_f / \partial r$ ratio is constant (constant heat flux between fracture fluid and formation), the solution to this equation evaluated at $z = 0$ can again be found using Laplace's transform:

$$T_e = T_{ei} + \frac{W c_w \sqrt{\alpha_e t / \pi}}{2\pi r \lambda_e} \frac{\partial T_f}{\partial r} \quad (42)$$

As in the previous section, Equation 42 results in a first-order ODE, where the unknown variable is the temperature of the fluid T_f :

$$\frac{dT_f}{dr} = -\frac{2\pi r \lambda_e}{W c_w \sqrt{\alpha_e t / \pi}} (T_f - T_{ei}) \quad (43)$$

The results of the ODE reads:

$$T_f(r, t) = T_{ei} + e^{-Ar^2} (T_{f,wb} - T_{ei}) \quad (44)$$

where $T_{f,wb}$ is the fluid temperature at the wellbore, and:

$$A = \frac{\pi \lambda_e}{W c_w \sqrt{\alpha_e t / \pi}} \quad (45)$$

3.3 Numerical modelling

This section aims to achieve two primary objectives. The first objective is to numerically model the sub-problems presented in Sections 3.2.1 and 3.2.2 in order to compare the analytical solutions with the results obtained from numerical simulations. The second objective is to model the entire FTES laboratory-scale experiment to obtain an initial estimation of the charging time for such a system.

3.3.1 FEniCS and workflow

All numerical models presented in this section were developed using **FEniCS** (Scroggs et al., 2022), which is an open-source computing platform designed for solving partial differential equations (PDEs) using the finite element method. The main advantage of **FEniCS** is that the user only needs to provide the weak forms, as all the matrix assembly is handled internally. Additionally, **FEniCS** provides users with greater control over the model compared to most other finite element software packages. For this project, all codes were developed using the Python interface of the latest version of the **FEniCS** Docker image, enabling them to be executed independently of the underlying hardware within the Docker container.

On the other hand, the Python API of **GMSH** software (Geuzaine and Remacle, 2009) was used to generate all the meshes. These meshes were then converted from .msh to .XDMF format using the Python **meshio** library. This file format can then be read directly from **FEniCS**.

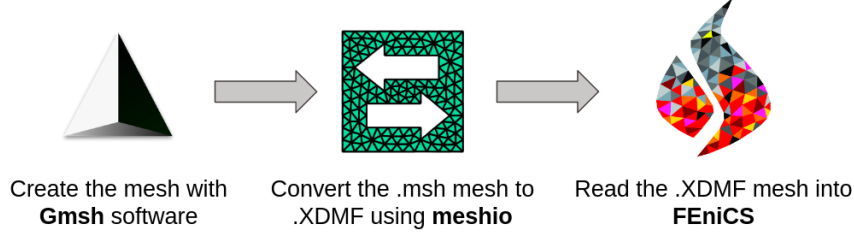


Figure 3.2: Workflow for mesh generation with Gmsh

Finally, the simulation results were written to an .XDMF file, which can be directly imported into **ParaView** software for analysis and processing.

3.3.2 Time discretization and weak formulation

Based on Equation 11, a general transient problem of heat diffusion-advection can be formulated as follows:

$$\rho c \frac{\partial T}{\partial t} + \rho_w c_w \mathbf{q} \cdot \nabla T - \nabla \cdot (\lambda \nabla T) = \gamma \quad \text{in } \Omega \times (0, t_{\text{final}}] \quad (46)$$

$$T = T^g \quad \text{in } \partial\Omega_T \times (0, t_{\text{final}}] \quad (47)$$

$$Q_i n_i = Q^g \quad \text{in } \partial\Omega_Q \times (0, t_{\text{final}}] \quad (48)$$

$$T = T_0 \quad \text{at } t = 0 \quad (49)$$

where T varies in both space and time. The boundary values T^g and Q^g could also depend on time.

The first step in solving a time dependent PDE is to discretize the time derivative, in order to transform the time dependent problem into a sequence of stationary problems that can be easily solved with the finite element method. Thus, at time t^{n+1} , Equation 46 becomes:

$$\rho c \left(\frac{\partial T}{\partial t} \right)^{n+1} + \rho_w c_w \mathbf{q} \cdot \nabla T^{n+1} - \nabla \cdot (\lambda \nabla T^{n+1}) = \gamma^{n+1} \quad (50)$$

In order to ensure stability, a backward difference is selected for the discretization of the time derivative (implicit scheme):

$$\left(\frac{\partial T}{\partial t} \right)^{n+1} \approx \frac{T^{n+1} - T^n}{\Delta t} \quad (51)$$

Substituting Equation 51 into Equation 50 reads:

$$\rho c T^{n+1} + \Delta t \rho_w c_w \mathbf{q} \cdot \nabla T^{n+1} - \Delta t \nabla \cdot (\lambda \nabla T^{n+1}) = \rho c T^n + \Delta t \gamma^{n+1} \quad (52)$$

The second step in solving the PDE is to turn the discretized equation (Equation 52) into its weak form, by multiplying both sides of the equation by a test function and integrating over the whole domain Ω . The test function must have zero value on the part of the boundary where Dirichlet boundary conditions are imposed, i.e. on $\partial\Omega_T$. Equation 52 thus yields:

$$\int_{\Omega} r \rho c T dV + \int_{\Omega} r \Delta t \rho_w c_w \mathbf{q} \cdot \nabla T dV - \int_{\Omega} r \Delta t \nabla \cdot (\lambda \nabla T) dV = \int_{\Omega} r \rho c T^n dV + \int_{\Omega} r \Delta t \gamma^{n+1} dV \quad (53)$$

After some simplifications, including an integration by parts, Equation 53 is reduced to:

$$a(r, T) = L_{n+1}(r) \quad (54)$$

with:

$$a(r, T) = \int_{\Omega} [r(\rho c T + \Delta t \rho_w c_w \mathbf{q} \cdot \nabla T) + \Delta t \lambda \nabla r \cdot \nabla T] dV \quad (55)$$

and:

$$L_{n+1}(r) = \int_{\Omega} r(\rho c T^n + \Delta t \gamma^{n+1}) dV + \int_{\partial\Omega} r \Delta t \lambda q^g dS \quad (56)$$

If the domain on which the PDE is being solved consists of multiple subdomains, such as multiple materials, the continuity condition at the interface between these subdomains is determined by the continuity of the temperature field and the continuity of the conductive heat flux. The continuity conditions at the interface of two subdomains A and B in perfect thermal contact at $\mathbf{x} = \mathbf{x}_0$ are therefore expressed as follows:

$$T_A(\mathbf{x}_0, t) = T_B(\mathbf{x}_0, t) \quad (57)$$

$$-\lambda_A \nabla T_A(\mathbf{x}_0, t) \cdot \mathbf{n} = -\lambda_B \nabla T_B(\mathbf{x}_0, t) \cdot \mathbf{n} \quad (58)$$

where $T_A(\mathbf{x}_0, t)$ and $T_B(\mathbf{x}_0, t)$ represent the temperatures in subdomains A and B at $\mathbf{x} = \mathbf{x}_0$, respectively, λ_A and λ_B denote the thermal conductivities of A and B, and \mathbf{n} is the normal vector to the interface between A and B at $\mathbf{x} = \mathbf{x}_0$.

The continuity of the advective flux is naturally ensured because both the fluid flow and temperature field are continuous at the interface between the subdomains. Consequently, it is imperative to ensure the continuity of the fluid flow during the analytical or numerical resolution of the fluid flow problem.

3.3.3 Code validation - Energy balance

One way to verify the proper implementation of the code is to perform an energy balance at each time step to ensure that energy is not artificially created or lost within the domain. Therefore, at each time step, the cumulative input and output energies should be computed, and the difference between these two quantities should be equal to the energy stored within the system.

Based on Equation 8, the advective energy given to the system across a boundary $\partial\Omega$ of the domain during a time period Δt can be calculated numerically as follows:

$$Q_{adv} = \int_{\partial\Omega} \Delta t \rho_w c_w \mathbf{q} \cdot \mathbf{n} (T_n - T_i) dS \quad (59)$$

where T_n is the temperature at time step n , T_i is the initial temperature, Δt is the time step, \mathbf{q} is the fluid velocity, and \mathbf{n} is the normal to the boundary. The advective energy that leaves the system can be calculated exactly in the same way, on the boundary corresponding to the outgoing fluid flux.

On the other hand, the energy given to the system by conduction during a time period Δt can be calculated based on Equation 9:

$$Q_{cond} = \int_{\partial\Omega} \Delta t \lambda_w \nabla T_n \cdot \mathbf{n} dS \quad (60)$$

However, this expression is only valid if the conductive heat flux is normal to the surface, which is not necessarily the case at a Dirichlet boundary. In such cases, the numerical integration becomes more challenging since the tangential conductive heat flux at the surface needs to be taken into account.

Finally, the energy stored within the system at each time step can be computed as follows:

$$Q_{stored} = \int_{\Omega} \rho c (T_n - T_i) d\Omega \quad (61)$$

If the domain is divided into several subdomains, then this integral must be calculated for each subdomain, taking into account the physical properties (ρ , c) of the material of the respective subdomain. These integrals must then be summed to obtain the total energy over the entire domain.

In the subsequent analysis, the calculation and evolution of these various energy components are illustrated using a classic wellbore heat transfer problem. For instance, we simulate the upper part of the block used in the FTES experiment, which includes only the well and the surrounding rock. The fluid flows vertically through the well at a constant velocity, and the velocity profile is assumed

to be uniform (Poiseuille average). The inlet water temperature is set to 70 °C (Dirichlet boundary condition), while the initial temperature of the block is 20 °C. All other boundaries of the domain are natural boundary conditions, meaning that there is zero conductive heat flux normal to these boundaries. However, there may be advective heat transfer occurring at these boundaries, allowing heat to exit the domain.

Table 3.1: Material parameters of the numerical model

Material	Water	Steel	Epoxy	Gabbro
Density ρ [kg/m ³]	997	8000	1100	3000
Specific heat c [J/(kg·K)]	4182	420	1110	460
Thermal conductivity λ [W/(m·K)]	0.598	45	0.14	2.15

The wellbore cross-sectional geometry is shown in Figure 3.3a, and its associated meshing is shown in Figure 3.3b. The 2D structured mesh was extruded along the z-axis to obtain a 3D mesh of height h . Additionally, the inner tube, through which the fluid circulates, was extruded an additional one millimeter to ensure that the conductive heat flux at the Dirichlet boundary is normal to the surface. This adjustment follows the previous discussion regarding the challenges in computing the conductive heat flux at boundaries of Dirichlet type.

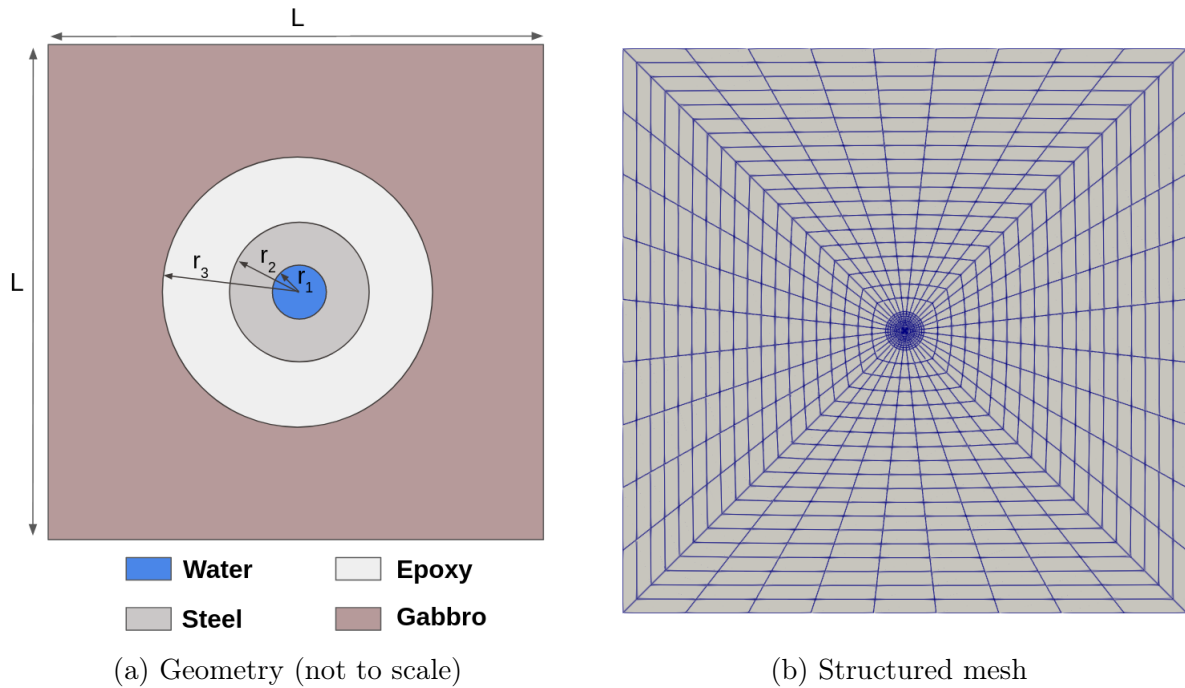


Figure 3.3: Cross-section geometry of the 3D mesh used for code validation

Table 3.2: Values of the geometrical dimensions illustrated in Figure 3.3a

Dimension	Value [mm]
r_1	0.5
r_2	1.6
r_3	8.5
L	250
h	125

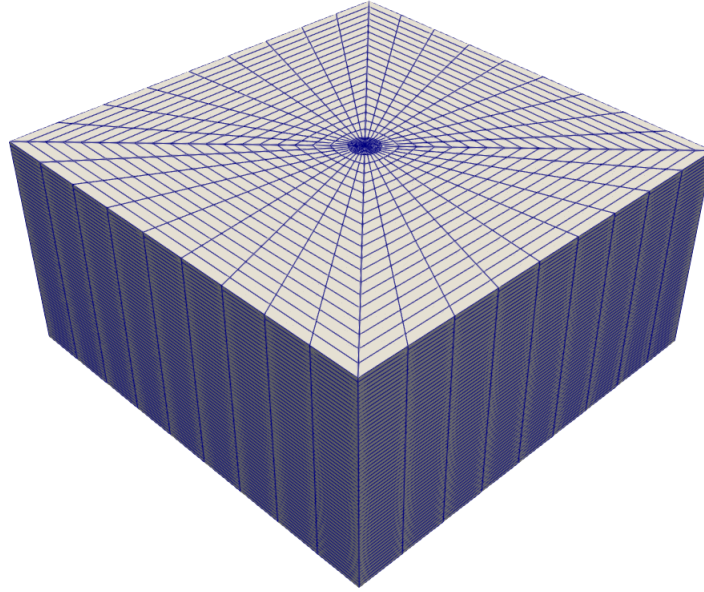


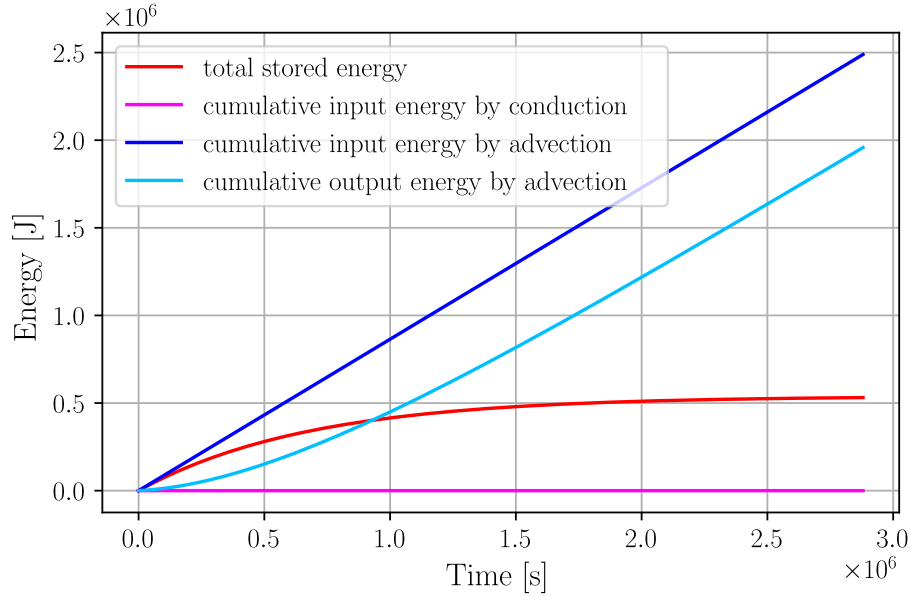
Figure 3.4: 3D mesh used for code validation

Regarding the mesh, two distinct types of elements were employed:

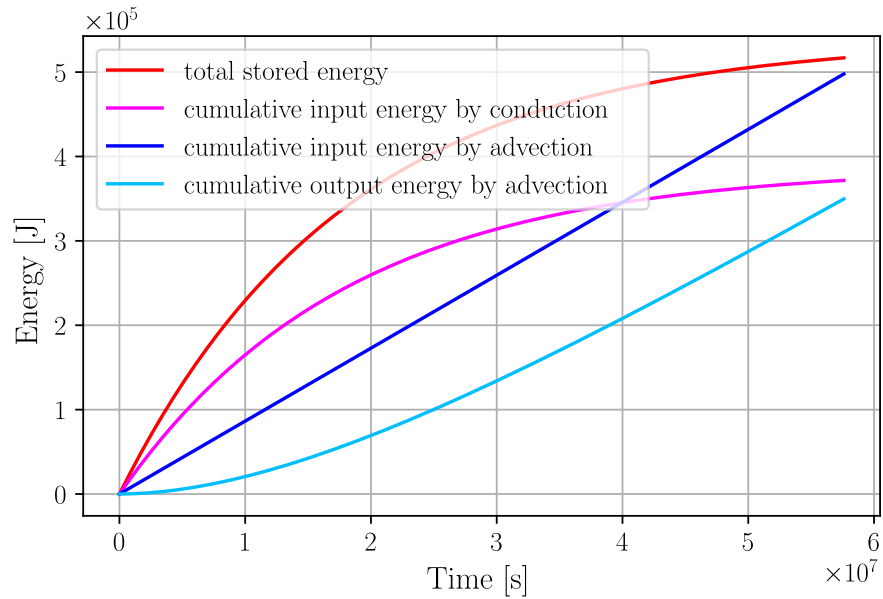
- **P1** Linear Lagrange elements for the temperature field.
- **DG0** Discontinuous Galerkin elements of degree 0 to define the different materials and the velocity field. These elements are convenient as they contain only one DOF (degree of freedom), enabling the assignment of a distinct material parameter or flow vector value for each element.

In the first simulation, for a flow rate of 0.25mL/min, Figure 3.5a shows that almost all the energy supplied to the system is provided by advection. Indeed, the velocity of the hot fluid entering the system at the Dirichlet boundary is sufficiently high to make the energy supplied by conduction negligible. Furthermore, from approximately one month onwards, the stored energy reaches a plateau, indicating that the entire block is at 70 °C. On the contrary, in the second simulation where the fluid

flow rate is 100 times smaller, Figure 3.5b shows that almost all the energy supplied to the system is provided by conduction. This result is rather intuitive because the lower the fluid velocity, the closer we get to a pure heat diffusion problem. In the long term, both simulations converge to the same stored energy value given by $E = V\rho c\Delta T$, where $\Delta T = 70 - 20 = 50\text{ }^{\circ}\text{C}$ and V is the total volume of the domain. However, the faster the fluid flow rate, the more rapidly this value is approached.



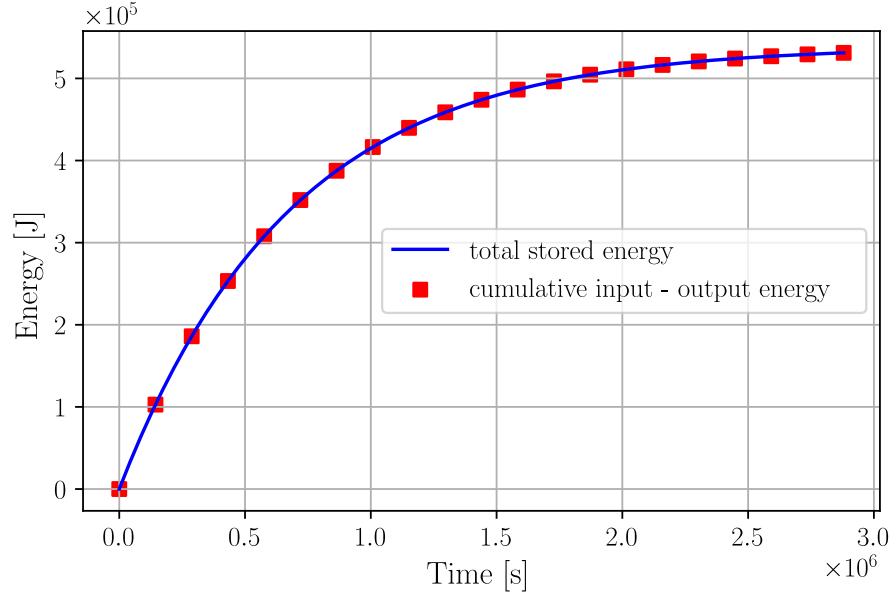
(a) Water flow rate $Q = 0.25\text{ mL/min}$



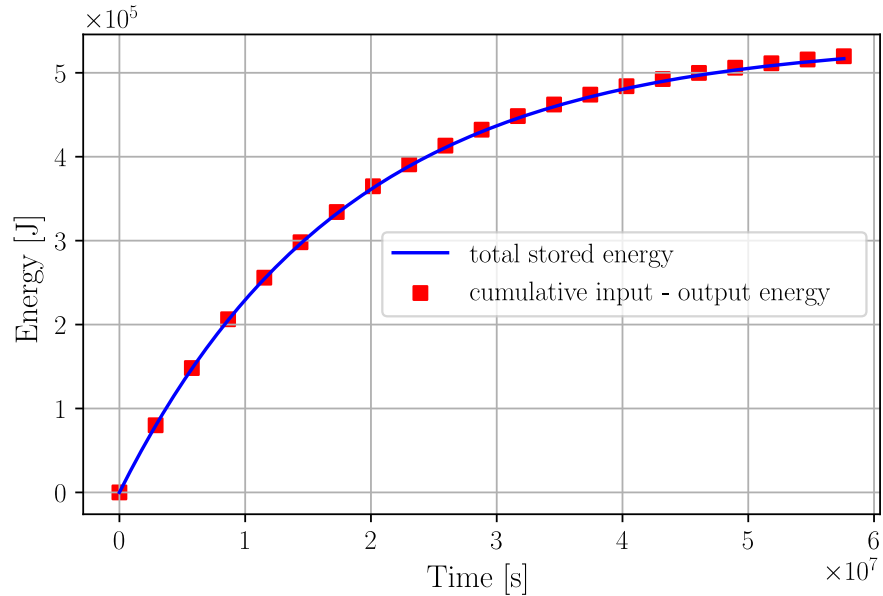
(b) Water flow rate $Q = 0.0025\text{ mL/min}$

Figure 3.5: Evolution of the different energy components with time

Finally, Figure 3.6 shows that in both simulations, energy is well conserved at each time step. Indeed, the energy stored in the domain at each time step is equal to the cumulative energy input to the system through conduction and advection at the top of the well, minus the cumulative energy that has exited the system through advection at the bottom of the well. This confirms the energy conserving property of the proposed model.



(a) Water flow rate $Q = 0.25$ mL/min



(b) Water flow rate $Q = 0.0025$ mL/min

Figure 3.6: Comparison of energy given to the system vs energy stored within the system over time

3.3.4 Heat transfer around wellbore

The objective of this section is to compare the analytical solution presented in Section 3.2.1 with the numerical model developed with FEniCS. For this purpose, the numerical model presented in the previous section is reused, as it already incorporates the modeling of heat transfer around a wellbore. The only change made to the model is the expansion of the dimensions L and h of the mesh to represent an infinite formation ($L' = 100 \cdot L$) and a slightly deeper well ($h' = 2 \cdot h$). The overall heat transfer coefficient of the wellbore is calculated as follows:

$$\frac{1}{U} = \frac{r_1 \ln(r_2/r_1)}{\lambda_{steel}} + \frac{r_1 \ln(r_3/r_2)}{\lambda_{epoxy}} \approx 166.5 [W/m^2K] \quad (62)$$

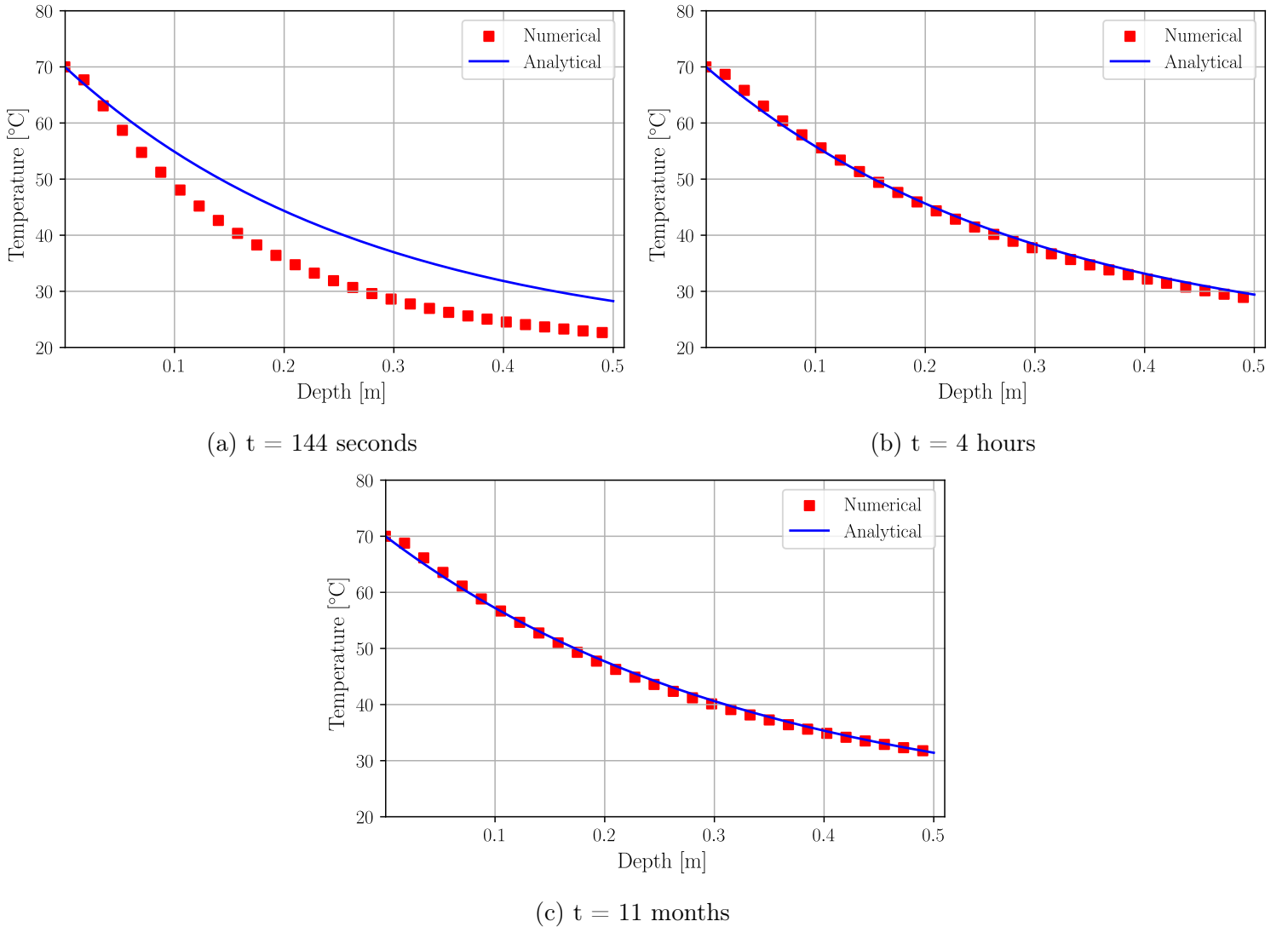


Figure 3.7: Comparison of analytical and numerical solutions for wellbore fluid temperature at different times (water flow rate $Q = 2$ mL/min)

The figures 3.7a, 3.7b, and 3.7c show the evolution of the fluid temperature along the well for different times. At the beginning of the simulation, for times close to the characteristic advection time $t_{adv}^* = h'/q$, the numerical solution deviates significantly from the analytical solution proposed by Hasan and Kabir (1991). Indeed, at early stages, the assumption that the accumulation term is negligibly small, which was used to develop the analytical solution, is not valid. However, as time advances and becomes much greater than t_{adv}^* , the analytical and numerical solutions converge.

3.3.5 Heat transfer along fracture

The objective of this section is to compare the numerical model developed using FEniCS with the analytical solution derived in Section 3.2.2. As a reminder, Section 3.2.2 investigates the heat transfer along a 2D fracture embedded in a 3D formation, where hot fluid flows radially from a central well. Therefore, the mesh needs to be adjusted to include a planar fracture perpendicular to the well. Currently, FEniCS does not support mixed meshes, allowing only one cell type of a single dimension. Thus, the fracture was discretized using thin volume elements.

To generate the 3D mesh, a 2D mesh similar to that of Sections 3.3.3 and 3.3.4 was first generated, representing the cross-section of the 3D domain perpendicular to the well. However, since this part solely focuses on the heat transfer along the fracture, the interior of the tubing was not meshed. The 2D mesh was then extruded in three steps. The first extrusion corresponds to the lower part of the block, located below the fracture. This extrusion was performed such that the thickness of the extruded elements decreases with height, resulting in a finer mesh near the fracture. The total height of this initial extrusion is denoted as h'' . In the second step, the top surface of the newly created volume was extruded to a height of e in order to generate the fracture volume ($e \ll h''$). Finally, a third extrusion was performed to create the volume corresponding to the upper part of the block. Similar to the first volume, the height of the third extruded volume is h'' , and its extrusion was done such that the thickness of the extruded elements are thinner near the fracture.

At each extrusion, distinct volume subdomains and surface boundaries were labeled by assigning Gmsh Physical Groups. This allows for the subsequent definition of materials and boundary conditions in the FEniCS code. In this section, since the interior of the metal tubing is not meshed, the inner surface of the tubing was used to set the inlet water temperature entering the fracture (Dirichlet boundary condition).

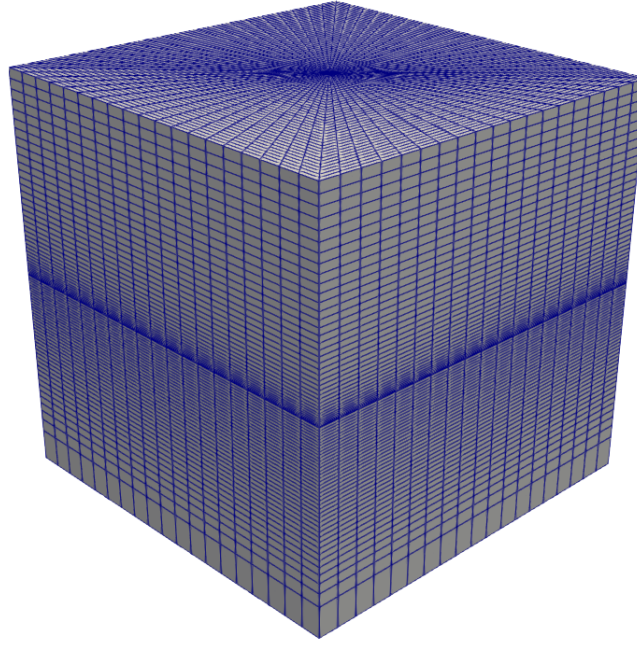


Figure 3.8: 3D mesh used for modelling of heat transfer along the fracture

The analytical model developed in Section 3.2.2 considers a fracture embedded in an infinite rock formation. Therefore, the analytical and numerical solutions can only be compared until the heat diffusion front reaches the boundaries of the numerical simulation domain. After this point, boundary effects become too important and the comparison is no longer valid. Consequently, as in the previous section, the dimensions L and h of the mesh should be increased in order to compare the two solutions over a longer period of time. In the preceding section, the domain dimension L was expanded ($L' = 100 \cdot L$) without increasing the number of elements since there is only diffusion in the radial direction to the well axis. Indeed, diffusion remains numerically stable even with relatively large elements. However, in this part, advection occurs within the fracture, requiring that the size of the elements in the plane perpendicular to the well does not exceed a certain threshold to avoid numerical instabilities. The maximum element size is limited by the numerical Péclet number, which must remain below 1. Hence, in this section, to prevent an excessive computational time, the mesh dimensions L'' and h'' were set to $L'' = 2 \cdot L$ and $h'' = 2 \cdot h$, respectively. This implies that the numerical and analytical solutions will deviate from each other after a specific time period, as the heat diffusion front reaches the boundaries of the domain.

In Section 3.3.4, since the tubing radius remains constant along the well, the fluid velocity was constant for all mesh elements within the tubing. However, in this section, the fluid flows radially from the well. Assuming steady flow, the fluid velocity vector is thus computed for each mesh

element within the fracture as follows:

$$\mathbf{q} = \frac{Q_{inj}}{2\pi re} \hat{\mathbf{r}} \quad (63)$$

where Q_{inj} is the total fluid flow rate injected at the borehole, r represents the distance from the center of the well to the centroid of the mesh element, $\hat{\mathbf{r}}$ is the unit vector indicating the direction of flow at the centroid of the mesh element, and e denotes the width of the fracture. The precise thickness of the fracture is unknown; however, for the purpose of this section and subsequent investigations, it has been assumed to be 500 microns.

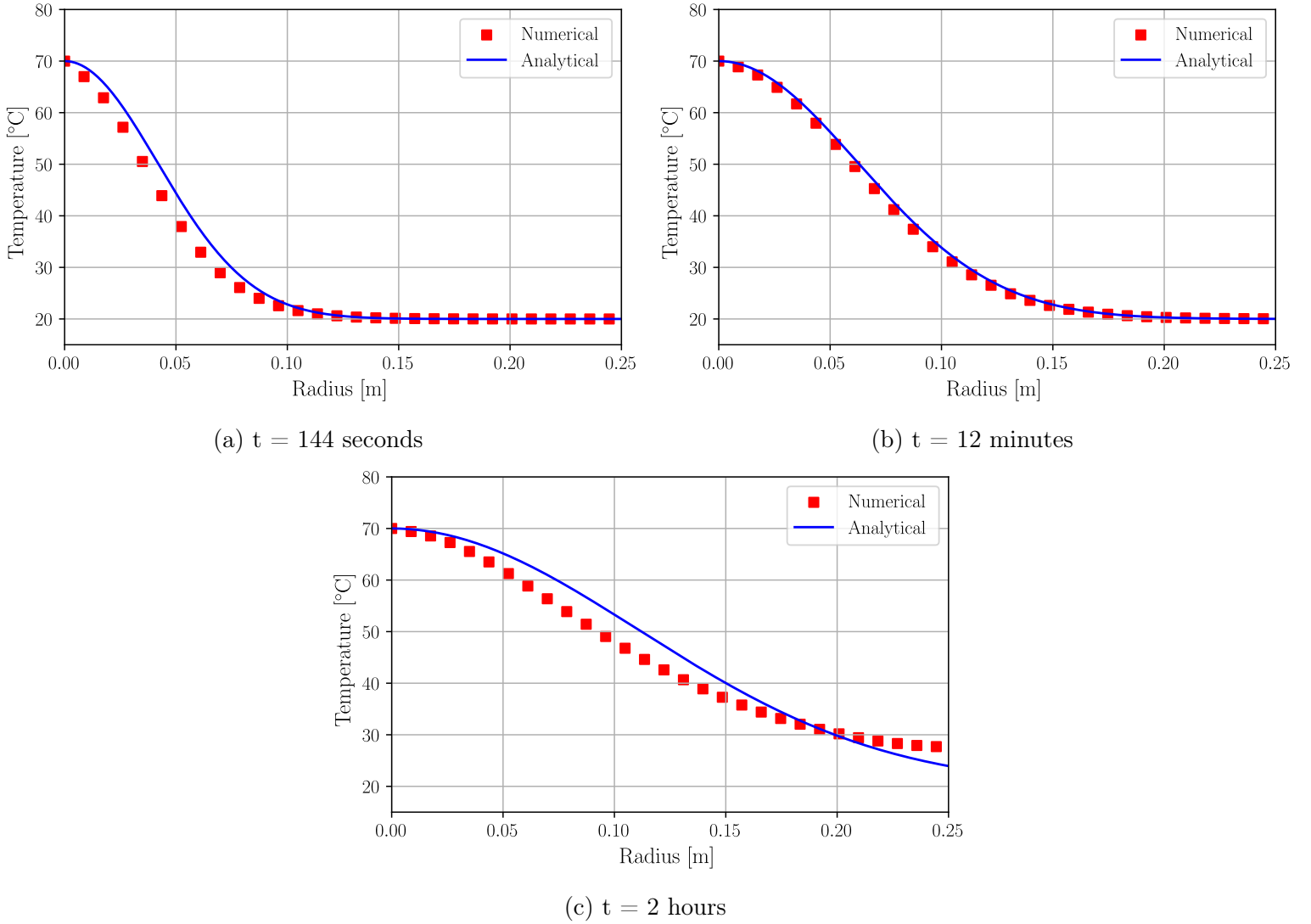


Figure 3.9: Comparison of analytical and numerical solutions for fracture fluid temperature at different times (water flow rate $Q = 20$ mL/min)

The figures 3.9a, 3.9b, and 3.9c show the evolution of the fluid temperature along the fracture for different times. As in the previous section, for times close to the characteristic advection time

$t_{adv}^* = h''/q$, the numerical solution deviates significantly from the analytical solution because the accumulation term cannot be neglected. As time advances and becomes greater than t_{adv}^* , the analytical and numerical solutions converge (Figure 3.9b). However, when the diffusive heat front reaches the boundaries of the domain, the two solutions diverge again (Figure 3.9c).

3.3.6 Modelling of FTES experiment

The objective of this section is to model the entire FTES experiment using the code developed with FEniCS, which has been previously validated against two analytical solutions. However, due to the fracture's finite dimensions and square shape, the assumption of purely radial flow is no longer valid and the workflow needs to be changed. Indeed, the square shape of the fracture will cause the radial flow to deviate near the boundaries. Furthermore, considering purely radial flow results in a total fluid quantity exiting the fracture that exceeds the injected fluid quantity, thereby violating mass conservation. Without mass conservation, the verification of energy conservation in heat transfer simulations is also compromised, as the energy leaving the system is significantly overestimated after a certain time. Hence, before proceeding with the heat transfer simulations, the fluid mass conservation equation needs to be solved to determine the precise fluid velocity field within the well and the fracture.

As a reminder, for steady-state flow, the fluid mass conservation equation within a fracture, referred to as the Reynolds equation in Section 3.1.1, reads:

$$\nabla \cdot \left(\frac{h^3(x, y)}{12\mu} \nabla p \right) = 0 \quad (64)$$

The input for heat transfer simulations is the fluid velocity field, which corresponds to the permeability of the medium multiplied by the gradient of the pressure field (the entire term included within the parentheses). Since a steady state is assumed, and only Neumann conditions are imposed, the fluid velocity is independent of the permeability of the medium. Therefore, the permeability can be fixed to the value of 1 for simplicity. However, if the values of the pressure field were to be studied for other applications, then the permeability should be calculated using the local cubic law or other analytical/empirical laws.

Taking these considerations into account, the new workflow for the numerical model involves the following steps:

1. A 3D mesh is generated using the GMSH Python API, and various physical groups are assigned to define the subdomains (materials) and boundary conditions.

2. The mesh is loaded into the FEniCS Python code.
3. A submesh is defined from the global mesh, which includes only the well and fracture subdomains.
4. On the submesh, the following steady-state problem is solved to find the fluid pressure at steady state:

$$\nabla^2 p = 0 \quad (65)$$

The fluid velocity field is then computed as:

$$\mathbf{q} = -\nabla p \quad (66)$$

5. The fluid velocity field is projected onto the parent mesh/global mesh.
6. The transient heat transfer problem, i.e., the advection-diffusion equation, is solved on the parent mesh.

To reduce the calculation time and since the mesh is symmetric, only one quarter of the domain is modeled. The global mesh and the submesh used for the modeling are shown in Figure 3.10. Furthermore, the dimensions of the domain are given in Table 3.3.

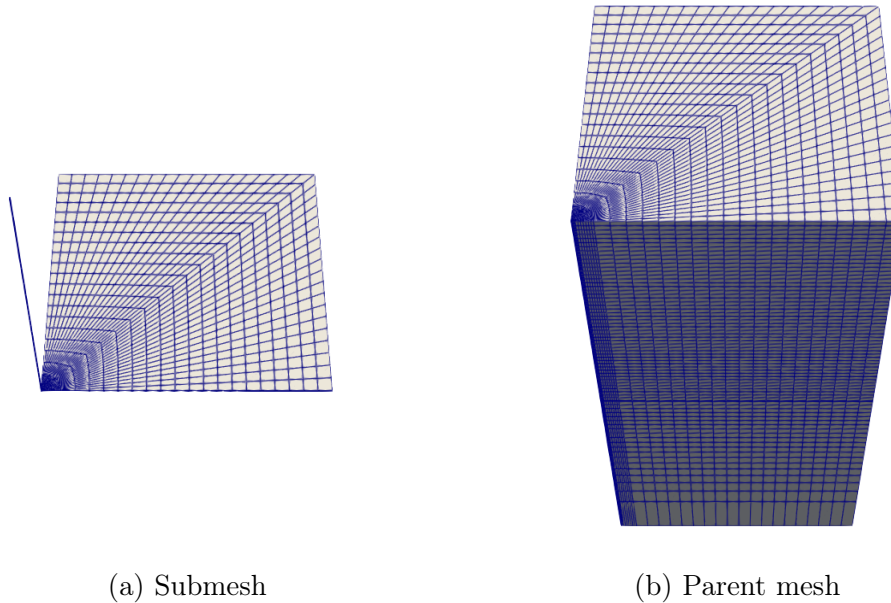


Figure 3.10: Structured meshes generated for the resolution of the flow and heat transfer problems

Table 3.3: Geometrical dimensions of the FTES experiment numerical model

Dimension	Value [mm]
L	125
h	125
e	0.5
h_{tot}	250.5

To address the flow problem, two types of boundary conditions are applied. At the entrance of the tubing, the fluid velocity is prescribed (Neumann boundary condition), while on the two thin surfaces representing the trace of the fracture on the two faces of the block, the pressure is set to zero (Dirichlet boundary condition). Therefore, the fluid enters at the wellhead and exits exclusively through the fracture boundaries, as the remaining surfaces have natural boundary conditions. On the other hand, for the heat transfer problem, the only prescribed boundary condition is the temperature of the water entering the block (Dirichlet boundary condition). All other boundaries of the domain have natural boundary conditions, implying that there is no conductive heat flux normal to these boundaries.

First, the impact of flow problem resolution accuracy on the solution of the heat transfer problem was investigated. This was achieved by solving the flow problem using different interpolation orders for the mesh elements and assessing the influence of each interpolation order on the energy balance of the heat transfer problem. Specifically, the steady flow problem was solved on the submesh using three different orders of interpolation for the pressure field (orders 2, 3, and 4). Then, the transient heat transfer problem was solved using order 1 mesh elements for the temperature field. The energy stored within the system, along with the different input and output energies, was finally computed as functions of time and depicted in Figure 3.11.

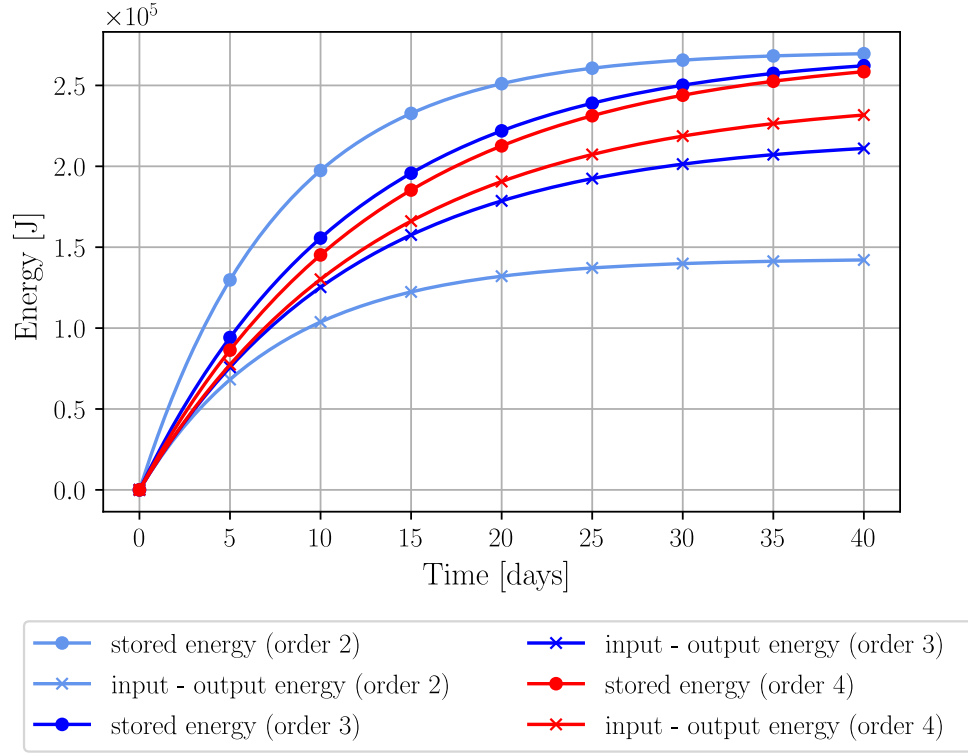


Figure 3.11: Influence of the interpolation order for the fluid pressure field on the solution of the heat transfer problem (utilizing order 1 interpolation for the temperature field)

The Figure 3.11 shows that the accuracy of the flow problem solution has a strong impact on the subsequent solution of the heat transfer problem. For instance, when solving the flow problem using second-order elements for pressure, the velocity flow field is of first-order, and the amount of fluid leaving the domain is slightly lower than that entering the system at the wellhead (with a relative error of 0.11%). The amount of fluid leaving the domain is computed by integrating the fluid velocity field over the two fine surfaces corresponding to the fracture trace on the faces of the block. This discrepancy between the incoming and outgoing fluid quantities leads to an overestimation of the energy stored within the domain and consequently, an overestimation of the outgoing energy. Therefore, the two cyan curves in Figure 3.11, which respectively depict the stored energy and the energy input minus output to the system, diverge significantly. However, as the interpolation order of the elements increases, the two curves converge. In order for both curves to match perfectly, further refinement of the mesh would be required. Such refinement would lead to a substantial increase in computation time and consequently, in the subsequent analysis, an interpolation order of 4 is chosen to solve the flow problem. The energy stored within the system will thus be slightly overestimated.

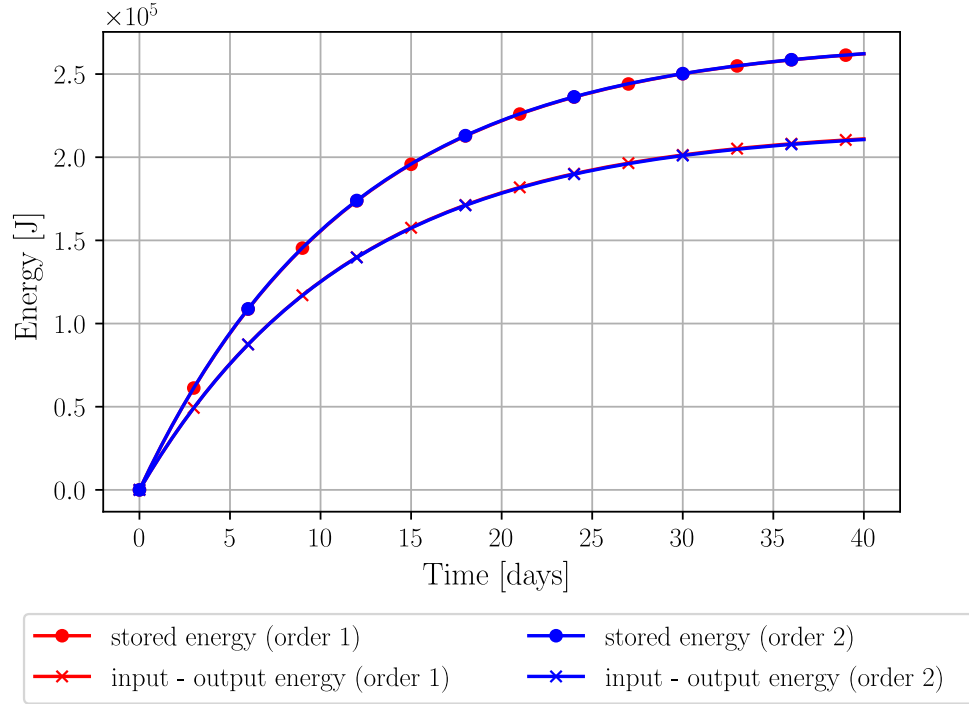


Figure 3.12: Influence of the interpolation order for the temperature field on the solution of the heat transfer problem (utilizing order 3 interpolation for the fluid pressure field)

The effect of the interpolation order of the mesh elements for the temperature field has also been investigated, and its influence on the solution of the heat transfer problem is shown in Figure 3.12. The results indicate that the interpolation order of the temperature field has a negligible impact on the solution. Therefore, the accuracy of the solution of the flow problem is the key element for achieving an accurate resolution of the heat transfer problem.

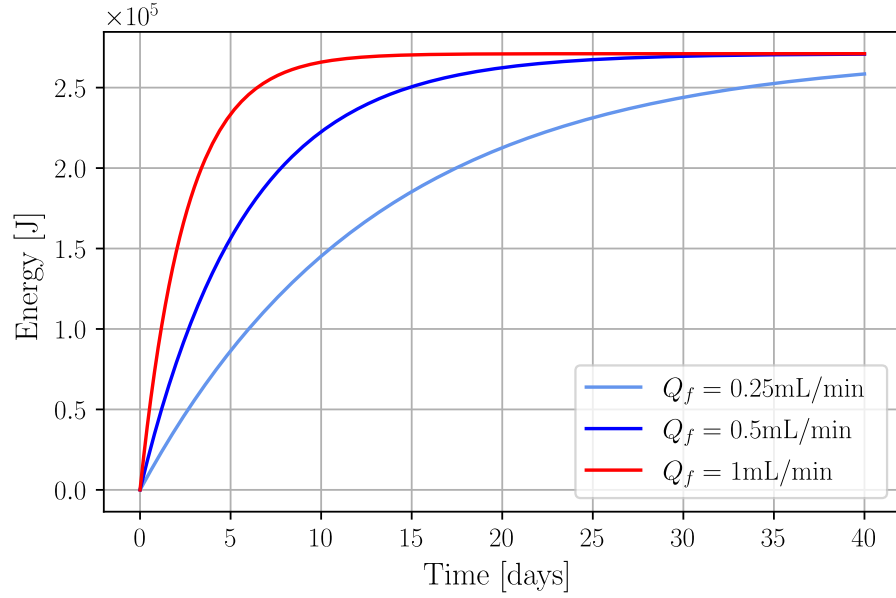


Figure 3.13: Influence of fluid flow rate on the charging rate of the FTES system

Following these considerations, three different simulations were conducted to assess the impact of the prescribed fluid flow rate on the charging rate of the system. The results demonstrate that increasing the flow rate leads to a significantly accelerated system charging (Figure 3.13), which is consistent as advective energy input to the system increases with flow rate.

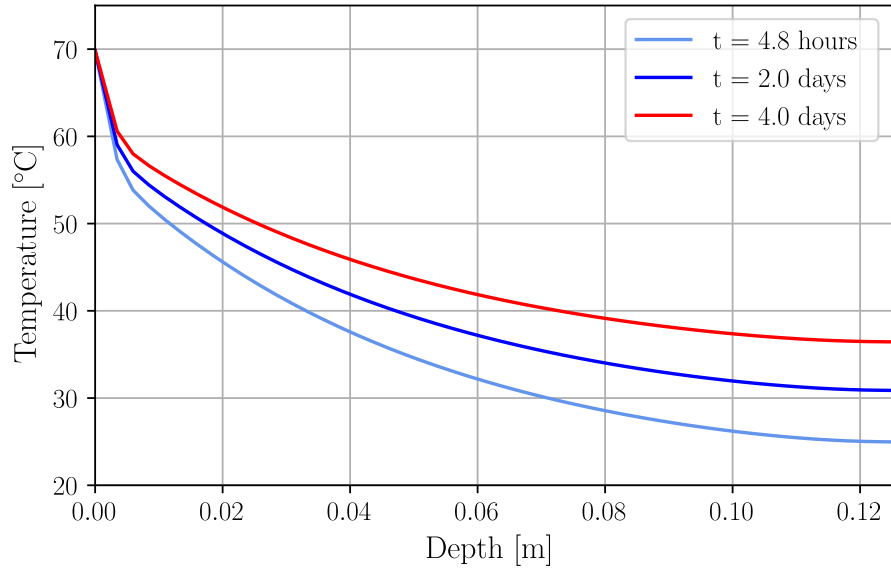


Figure 3.14: Evolution of the temperature along the well with time

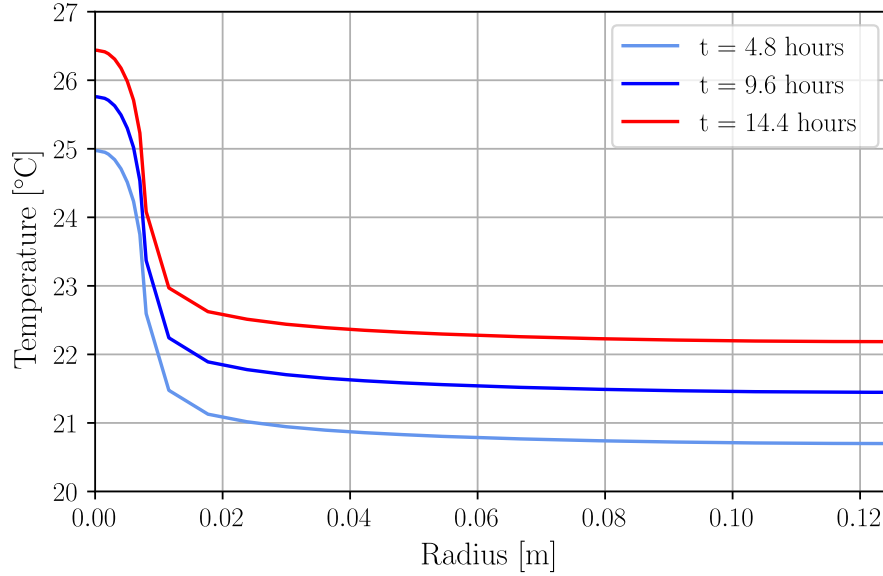


Figure 3.15: Evolution of the temperature along the fracture with time

Then, the evolution of temperature inside the wellbore over time was investigated, and the results are shown in Figure 3.14. As expected, the water temperature within the wellbore follows an exponential decay. At a flow rate of 0.25 mL/min, the water has already dissipated nearly all of its heat by the time it reaches the fracture. It may appear counterintuitive that water, flowing at an approximate speed of 5.3 mm/s inside the well, can reach the bottom of the well with a temperature close to that of the rock formation. However, it is important to understand that the key parameter that drives the heat transfer is not the fluid velocity but the mass flow rate, as mathematically shown in Section 3.2.1. Thus, if the diameter of the tube were twice as small, the fluid velocity within the tube would be four times higher, but since the flow rate remains the same, the temperature profile within the well would also be the same. Ultimately, what matters is not the fluid velocity but the rate of energy given to the system.

Similarly, the Figure 3.15 shows that the water temperature decreases exponentially within the fracture (starting at $r = 8.5\text{mm}$ on Figure 3.15), although it is less pronounced as the temperature gradient is smaller. In Figure 3.15, between $r = 0\text{mm}$ and 8.5mm , the temperature profile has a concave shape, which is not related to the "S" shape observed in the temperature profile at Section 3.3.5, but is rather due to the change in fluid flow direction as it transitions from vertical flow in the well to horizontal flow within the fracture.

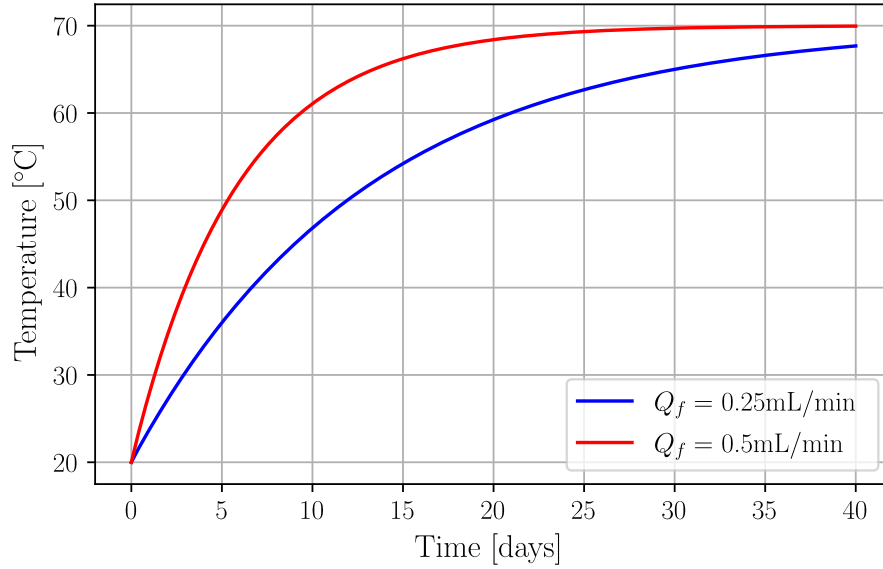


Figure 3.16: Evolution of the temperature at point A with coordinates (0.125, 0, 0.188) over time

In the following sections of this report, it will be shown that for the FTES laboratory-scale experiment, the fluid flow rate injected by the pump can hardly exceed 0.25 mL/min due to the very low transmissibility of the fracture. Therefore, it is important to discuss the time required to experimentally detect significant temperature variations on the faces of the block. For this purpose, the temperature evolution at point A, located on the east face of the block 6.25 cm above the fracture trace, was monitored and plotted in Figure 3.16. The results demonstrate that to detect a significant temperature variation ($\Delta T > 5^\circ\text{C}$) on the surface of the block, a minimum period of 2-3 days is required. However, if the water flow rate were doubled, a significant temperature variation could be detected within a single day.

3.4 Discussion

Two approaches were discussed in the first part of the project. First, the mathematical approach decomposed the general problem into two heat transfer sub-problems: heat transfer around a well and heat transfer from a fracture. The two analytical solutions presented rely on a number of assumptions, such as the infinite dimension of the rock formation. These two solutions can therefore only be applied as long as the heat diffusion front has not reached the boundaries of the domain. For the design of experiments, simple mathematical models are preferable to complex numerical simulations, and these two models can therefore be used, for example, to obtain an initial estimate of the flow rate required for the temperature of the water entering the fracture to be sufficiently high.

Second, a numerical model was developed using FEniCS to simulate the laboratory-scale FTES

experiment. The numerical model was first compared with the two analytical solutions, before being used to analyse the operation of the FTES experiment. According to the model, for a fluid flow rate of 0.25mL/min injected by the pump, it would take at least 2 days before a significant temperature variation ($\Delta T > 5^{\circ}\text{C}$) is observed on the faces of the block. In addition, the model assumes zero heat flux on the block faces, which implies perfect block insulation. However, in practice, achieving such insulation is not feasible, and it is therefore likely to take approximately 3 days before a significant temperature variation is detected on the faces of the block. Finally, with a flow rate of 0.25mL/min, the heat transfer operates mainly from the well, which is not representative of a real scale FTES system, where the heat transfer should be mostly from the fractures to the rock formation.

4 FTES experiment

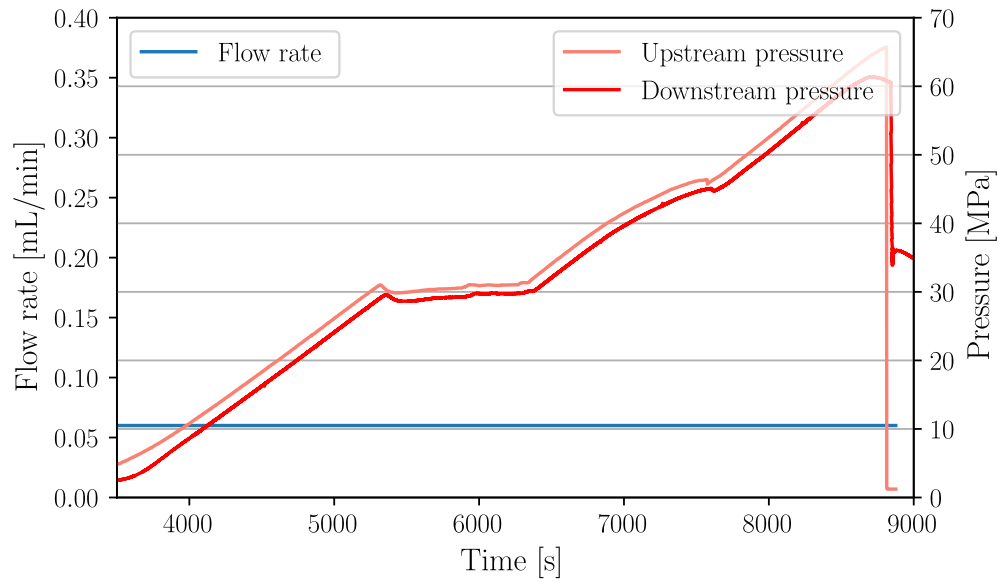
4.1 Fracture creation

4.1.1 Hydraulic fracturing experiment

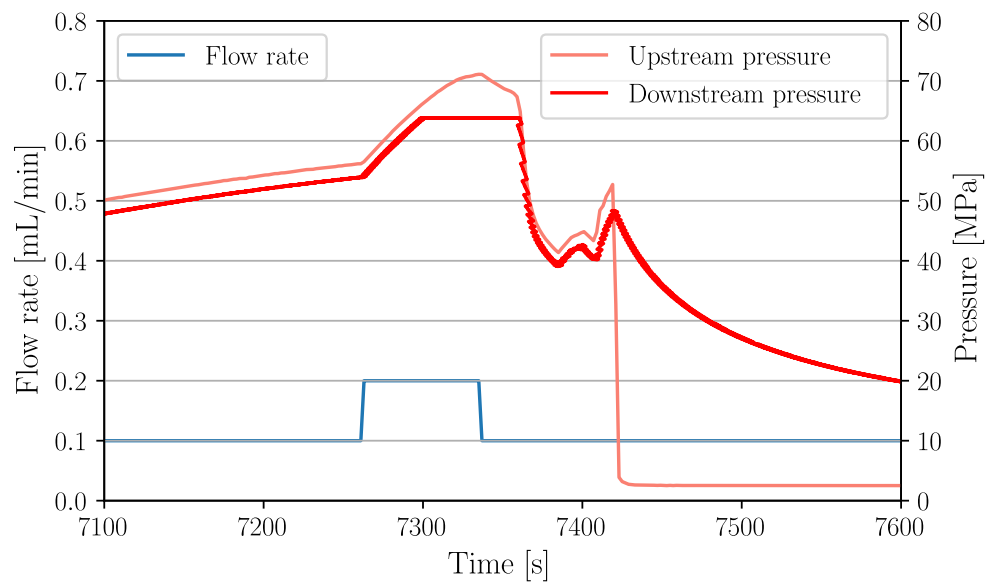
The gabbro block used for the laboratory-scale FTES experiment (GB08) was hydraulically fractured prior to the start of this work. The standard laboratory fracturing procedure requires the block to be placed within a triaxial press, which applies confinement in each of the three dimensions using symmetric pairs of flat jacks connected to a pressure-volume controller (Liu and Lecampion, 2022). Subsequently, a fracturing fluid is injected through the central well at a controlled flow rate regulated by the pump. Throughout the injection process, an acoustic imaging system integrated into the loading platens monitors the evolution of the fracture front over time.

The actual fracturing process of the gabbro block GB08 was more intricate. Indeed, to the best of the author’s knowledge, it is likely that epoxy resin infiltrated the notch when the completion tool was glued inside the wellbore. The fracturing of block GB08 was thus conducted on two different days, and the data collected are shown in Figure 4.1. In Figure 4.1, two pressure curves are depicted: upstream pressure represents the pressure measured by the pump, while downstream pressure corresponds to the pressure measured by a pressure sensor positioned downstream of the flow control valve. In the first experiment, the presence of epoxy in the notch prevented the rock from fracturing even under extremely high pressures (Figure 4.1a). Indeed, gabbros usually require pressures between 35 and 40 MPa to initiate a fracture. Acoustic data also indicated that only the epoxy fractured over a distance of slightly more than one centimeter. At one point, the pressure in the tubing became so high that the tubing line disconnected, resulting in the sudden pressure drop observed in Figure 4.1a at time $t \approx 8900$ s. It is likely that the fracture of the epoxy created pathways for fluid leakage within the wellbore.

In the second fracturing experiment, successful propagation of the main fracture in the gabbro was achieved. The pressure data in Figure 4.1b demonstrate that fracturing the gabbro also required very high pressures. The pressure plateau observed in the downstream pressure curve between times 7300 and 7375 seconds corresponds to the saturation of the pressure sensor, which is unable to measure pressures exceeding 64 MPa. Additionally, a complication arose with the recording of passive data, rendering only the active data suitable for analysis.



(a) First fracking experiment



(b) Second fracking experiment

Figure 4.1: Hydraulic fracturing of gabbro block GB08

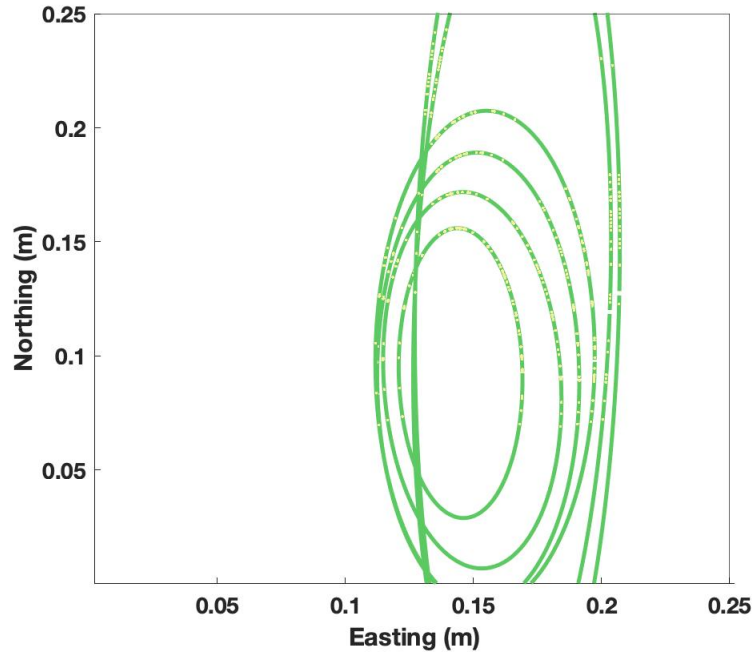


Figure 4.2: Visualization of fracture front propagation using acoustic emission data. The plot was generated by Dr. Seyyedmaalek Momeni, who performed the fracturing of the block.

The processing of active acoustic data (Figure 4.2) indicates that the fracture has predominantly developed in the eastern part of the block. Nevertheless, due to the limitations in the accuracy of the active data, it is not possible to precisely predict the exact position of the fracture within the block.

4.1.2 Fracture geometry

To reduce uncertainty regarding the fracture position within the block, the first step of this study involved mapping the fracture trace on the block faces. For this purpose, the coordinates of various points on this trace were collected and plotted in Figure 4.3. Subsequently, a cubic interpolation was performed between these points to gain insights into the azimuth and dip of the fracture.

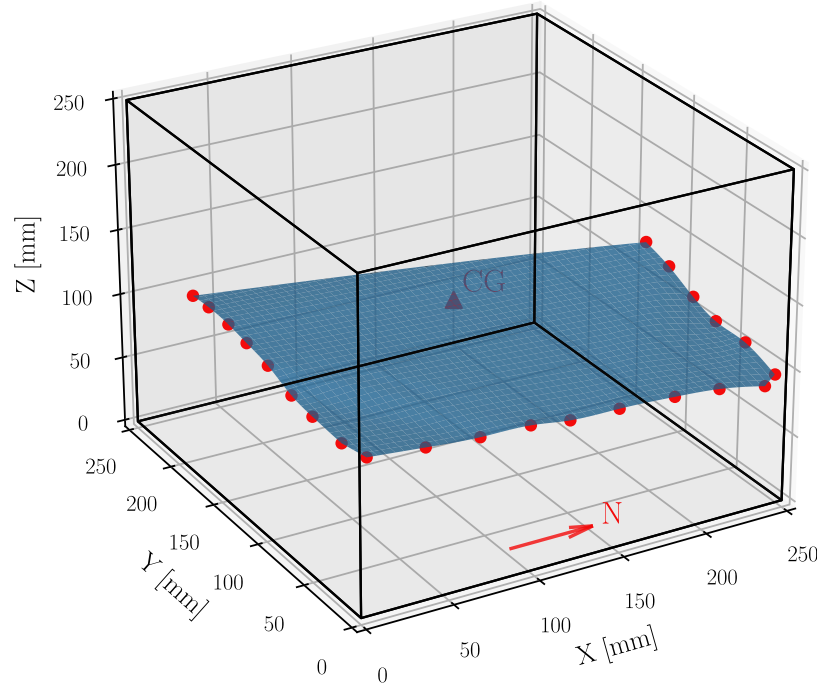


Figure 4.3: Estimation of fracture geometry through fracture trace data

Figure 4.3 confirms that the fracture primarily extends towards the east, with no visible trace of the fracture on the west side. Additionally, Figure 4.3 reveals a slight inclination of the fracture towards the northeast direction.

4.2 Transmissibility tests

The success of an FTES project primarily relies on the quantity and physical properties of the injected fluid, as well as the properties of the fractures. These aspects are inherently interconnected since, for example, a lower fluid viscosity could allow for higher quantities of injected fluid. In general, as explained in Section 3.1.1, there is limited flexibility in choosing the fluid, with water being prioritized due to its low cost and advantageous thermal properties. However, fractures can be designed to enhance fluid flow by implementing various techniques, including the injection of proppants during the hydraulic fracturing process.

The objective of this section is to estimate the transmissibility of the GB08 block fracture, whose geometry was presented in the previous section. Since the block was hydraulically fractured without proppant injection, the fracture thickness is very thin (a few microns) and is expected to vary

significantly with pressure. An analytical solution was presented in Section 3.1.1 for the calculation of fracture transmissibility. However, the solution requires the knowledge of the average fracture thickness, which is unknown for the GB08 block. This section therefore adopts an experimental approach to compute the transmissibility of a fracture based on injection flow rate and pressure data.

In its general form, the volumetric flow rate Q circulating through a fracture is directly related to the change in pressure across the boundaries of the flow domain ΔP through the following relationship (Renshaw, 1995):

$$Q = CT \frac{\Delta p}{\mu} \quad (67)$$

where C is a constant that depends on the geometry of the flow pattern within the fracture, μ is the fluid viscosity, and T is the fracture transmissibility. For steady radial flow from a well in an infinite homogenous medium, the constant C is given by:

$$C = \frac{2\pi}{\ln r_0/r_w} \quad (68)$$

where r_w is the well radius and r_0 is the radial distance to the constant pressure boundary, often referred to as the radius of influence. Similarly, for steady unidirectional flow over a distance L , the constant C is given by:

$$C = \frac{1}{L} \quad (69)$$

Since the fracture of the GB08 block is not perfectly horizontal nor uniformly extended in all directions, the flow is neither radial nor unidirectional, and the factor C is unknown. The order of magnitude of the fracture transmissibility can, however, be obtained using the following expression:

$$T \approx \frac{Q\mu}{\Delta p} \quad (70)$$

In order to determine the transmissibility of the GB08 block fracture, the block was connected to the ISCO pump, and a pressure transducer was placed near the entrance of the block. Since both the tubing length and the flow rate are small, the pressure measured by the transducer was assumed to be approximately equal to the pressure at the bottom of the well.

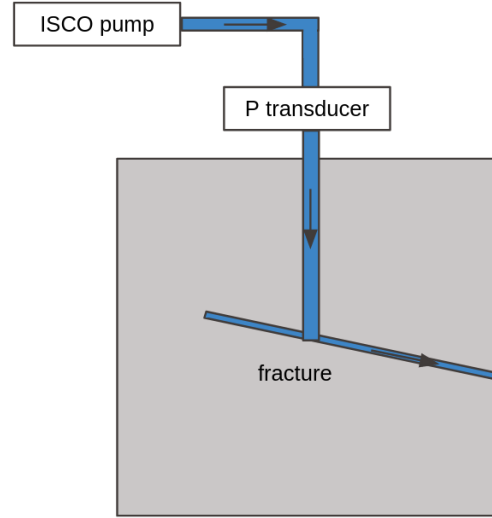


Figure 4.4: Experimental setup for fracture transmissibility estimation

The experiment could be conducted in two different ways: either by imposing the flow rate using the pump and measuring the pressure within the tubing using the pressure transducer, or by imposing the pressure in the tubing using the pump and recording the flow rate required to maintain that pressure constant with the same pump.

The first approach was initially chosen due to its better control over the experiment in the event of a new fracture initiation during the high-pressure injection process. To assess the overall transmissibility of the fracture, a series of flow rate stages were applied by the pump, while monitoring the pressure with the pressure transducer. The objective was to wait for the pressure to stabilize (achieve steady flow) at each flow rate increment, thereby enabling the computation of fracture transmissibility using the stabilized pressure and the imposed flow rate values. However, the presence of elastohydrodynamic effects hindered pressure stabilization. Indeed, it is likely that the fracture only opens at a specific pressure. Once this pressure is reached, the fracture opens, expelling a certain volume of fluid, which results in a sufficient pressure drop for the fracture to close again. These cyclic effects are illustrated in Figure 4.5 for two different flow rates, highlighting that the frequency of these cyclic patterns increases with higher flow rates.

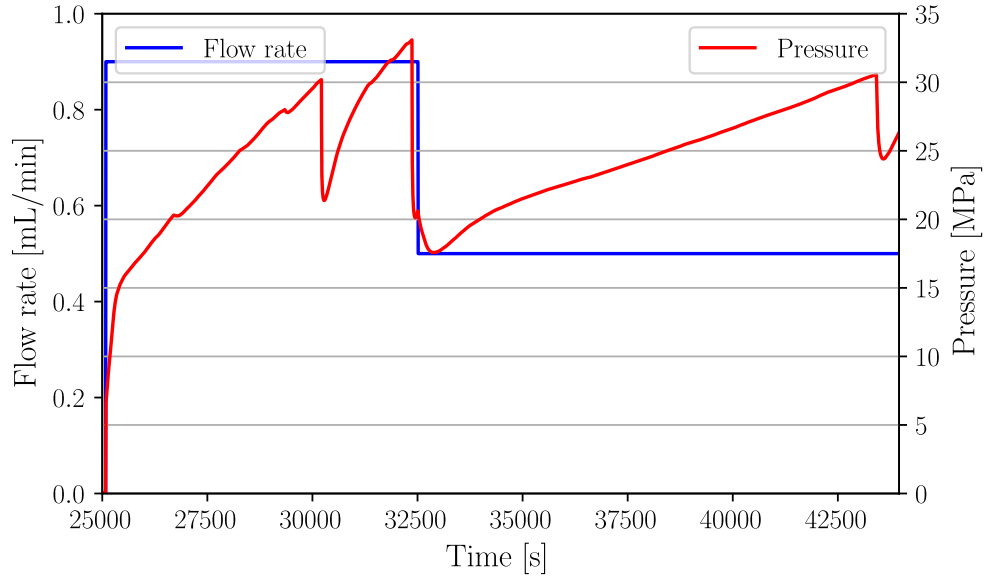
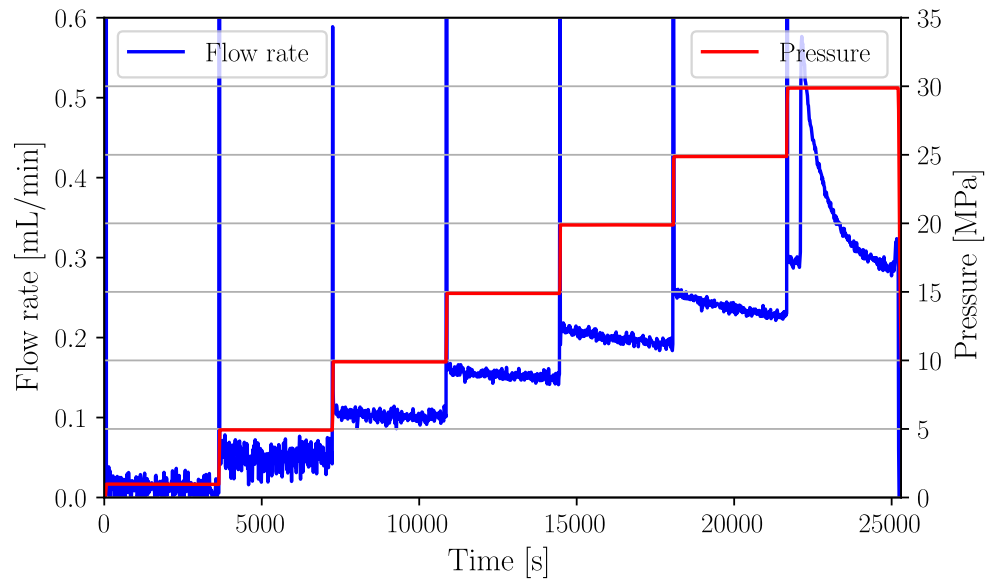


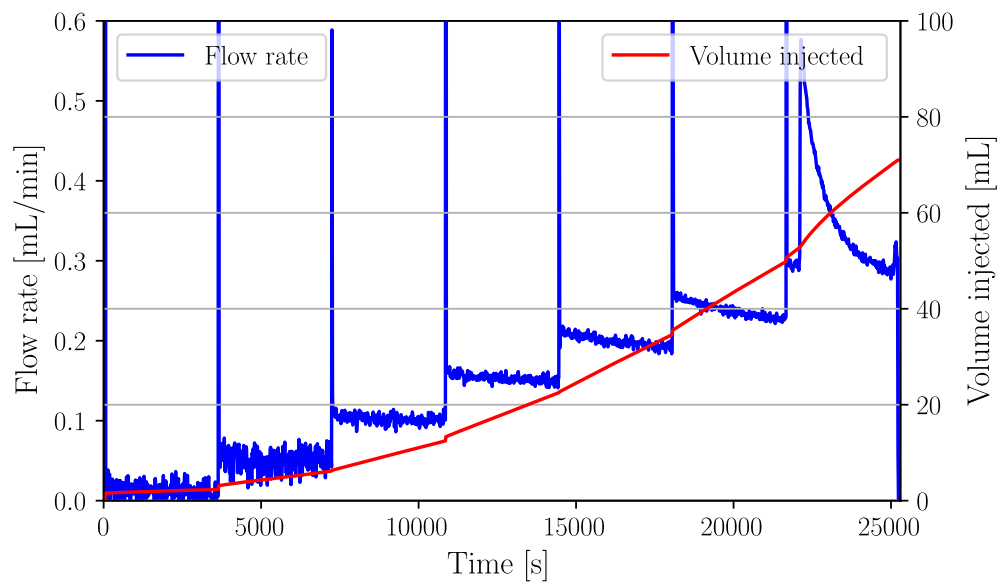
Figure 4.5: Observation of elastohydrodynamic effects when flow rate stages are imposed by the pump

To mitigate these effects, the reverse procedure was chosen. This second procedure involved applying different pressure stages using the pump while simultaneously recording the corresponding flow rates required to maintain each pressure increment. The results of this new procedure are shown in Figure 4.6 for pressure stages ranging from 1 to 30MPa. In order to mitigate noise in the flow rate data, the values were grouped in sets of 15. The impact of different group sizes on the visualization of fluid flow rate data is illustrated in Figure 4.7.

In Figure 4.6a, it can be observed that even under high pressures (>20 MPa), the injected flow rates remain significantly low. This observation suggests the presence of numerous bridges within the fracture (areas of the fracture that are still clogged), which hinder its opening when subjected to pressure. At a pressure of 30 MPa, Figure 4.6a shows a sudden increase in flow rate, followed by a gradual decline. This behavior likely corresponds to the failure of one or several of these bridges.



(a) Imposed pressure stages versus recorded flow rates



(b) Cumulative injected water volume versus recorded flow rates

Figure 4.6: Evolution of pressure, flow rate and injected water volume with time

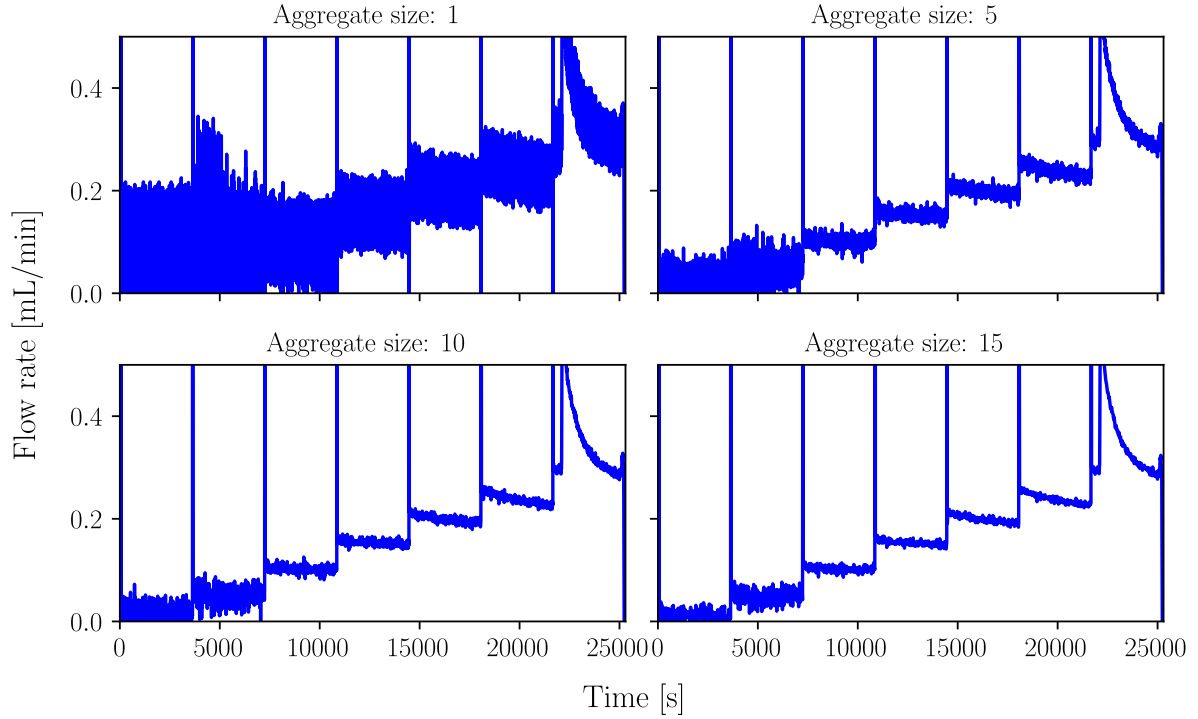


Figure 4.7: Impact of data aggregation group size on water flow rate data visualization

By selecting the final flow rate values in Figure 4.6 for each pressure stage, when the flow rate has stabilized or is nearly stabilized, the transmissibility can be computed using Equation 70. The transmissibility of the fracture as a function of pressure is shown in Figure 4.8. If the relationship between pressure and fracture aperture was linear, then the transmissibility of the fracture should increase cubically with pressure according to the cubic law (Equation 3). Here, the magnitude of transmissibility remains constant ($10^{-19} \text{ [m}^3\text{)]}$), confirming that certain regions of the fracture are still clogged.

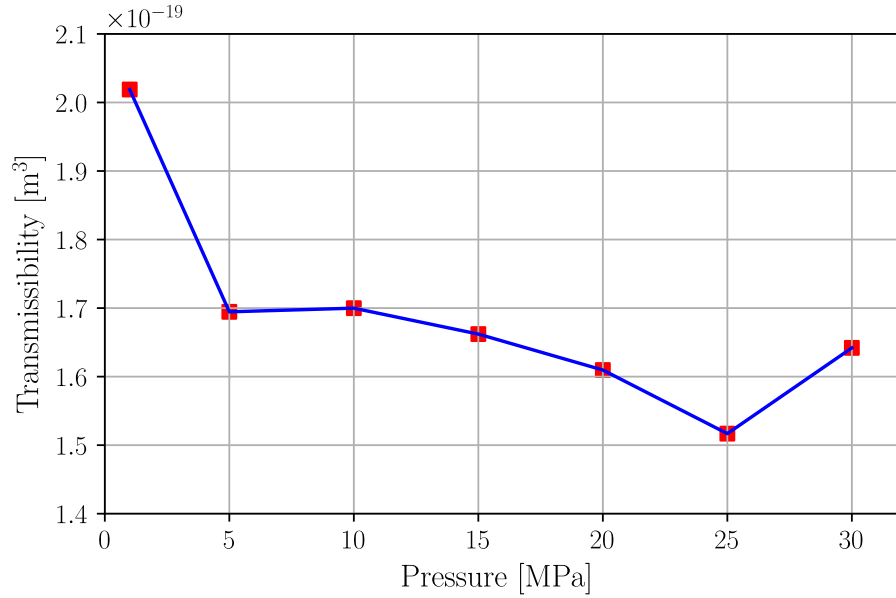


Figure 4.8: Evolution of fracture transmissibility with pressure

In order to further crack the fracture bridges and thus increase the fracture transmissibility, the pressure was increased to 35 MPa. This allowed for a further extension of the fracture towards the east, but unfortunately, it also led to the creation of a new fracture. The trace of the new fracture and the extension of the original fracture are shown by the violet dots in Figure 4.9.

Following the apparition of the new fracture, the transmissibility experiment was repeated. The results, presented in Figure 4.10, show that the transmissibility of the fracture increased by an order of magnitude. Experimentally, fluid was observed exiting the new fracture on the south face of the block, partly explaining the increase in transmissibility.

Subsequently, the trace of the new fracture was fully sealed with epoxy resin to ensure that flow through the fracture only occurred through the initial fracture, and the transmissibility experiment was conducted again. The results of this third experiment, also shown in Figure 4.10, indicate that the sealing of the new fracture led to a restoration of transmissibility levels comparable to those observed in the initial fracture ($10^{-19} \text{ [m}^3\text{]}$). The slight increase in transmissibility is likely due to the extension of the initial fracture, as shown in Figure 4.9.

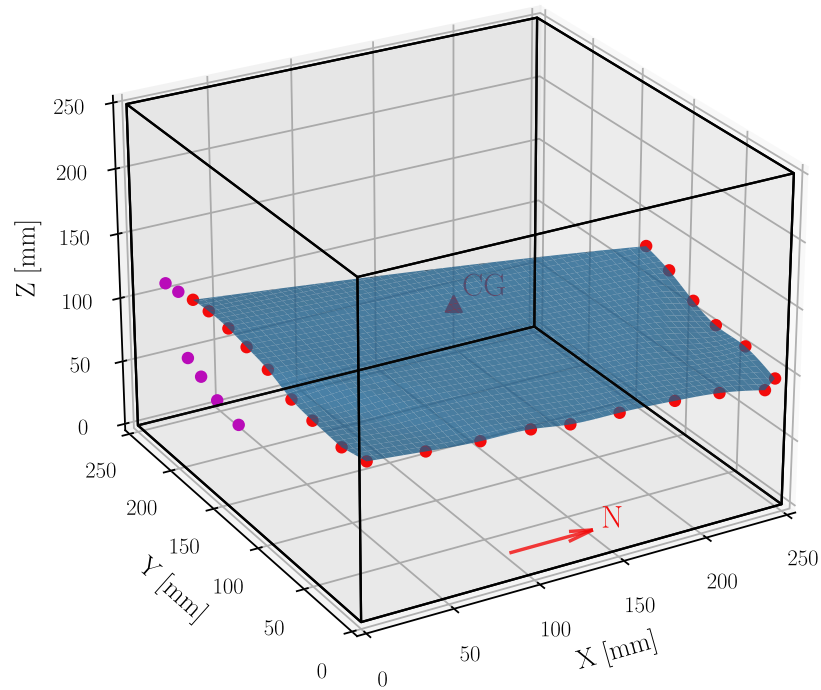


Figure 4.9: Geometry of the initial fracture extension and trace of the newly created fracture

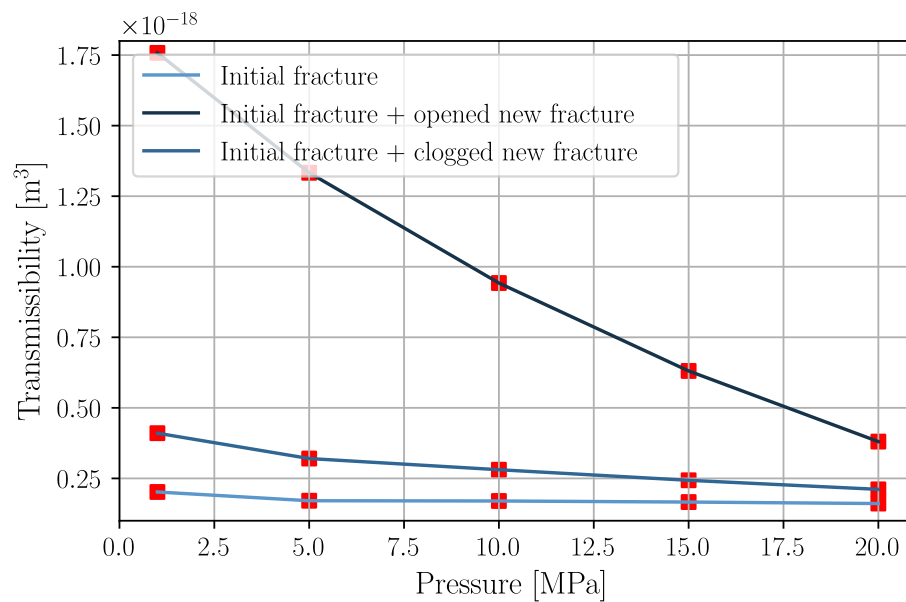


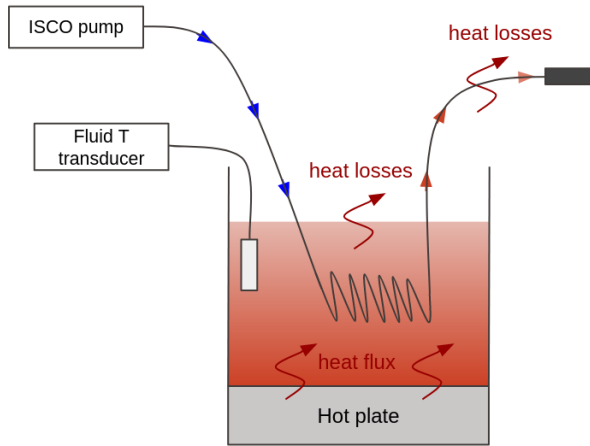
Figure 4.10: Comparison of transmissibility between the initial fracture, the initial fracture with the opened new fracture, and the initial fracture with the clogged new fracture

4.3 Heating system setup

The experimental setup for the heating system is shown in Figure 4.11. Its principle is as follows:

1. A beaker with a one-liter capacity is filled with silicone oil, which has a boiling point above 315°C.
2. The oil-filled beaker is placed on top of a hot plate, whose power can be adjusted using a slider.
3. At the level of the beaker, the tubing connecting the pump to the block is submerged in the oil and twisted into a coiled spiral shape, to maximize its contact surface area with the oil.
4. A thermistor-based fluid temperature sensor is placed inside the beaker to control the oil temperature. This sensor is connected to an Arduino board, which transmits the resistance data acquired from the sensor to the computer. A Python code then reads the data received from the board and converts the resistance values into corresponding temperatures.
5. The slider is adjusted to the appropriate level to heat the oil to the desired temperature. The fluid sensor monitors the temperature evolution of the silicone oil.
6. Once the oil temperature has stabilized at the desired level, the pump can begin injection.

The temperature of the water at the outlet of the heating system is influenced by two parameters: the power of the heater and the water flow rate regulated by the pump. Indeed, as the water flow rate increases, the heating time decreases, resulting in less time for the water to reach thermal equilibrium with the oil temperature.



(a) Schematic representation of the heating system setup



(b) Photograph of the experimental setup

Figure 4.11: Experimental setup for heating system

4.4 Configuration of fluid temperature at block inlet

Once the water injection and heating systems are set up, the next step is to configure the temperature of the water entering the block. In the previous section, it was demonstrated that the output temperature of the heating system depends on two parameters: the silicone oil temperature, which is determined by the power of the heater, and the water flow rate imposed by the pump. Additionally, the study conducted on fracture transmissibility (Section 4.2) has shown that even under high pressures, the flow rate that can be injected into the fracture does not exceed 0.3 mL/min. Therefore, in practice, the flow rate parameter range is very limited.

The purpose of this section is to investigate the impact of these parameters on the inlet water temperature of the block.

4.4.1 Non-pressurized injection

The initial setup of the FTES experiment is illustrated in Figure 4.12. In this setup, the block is positioned 1.1 meter away from the heating system, and at the midpoint of the tubing, there is a connector that can be opened as needed.

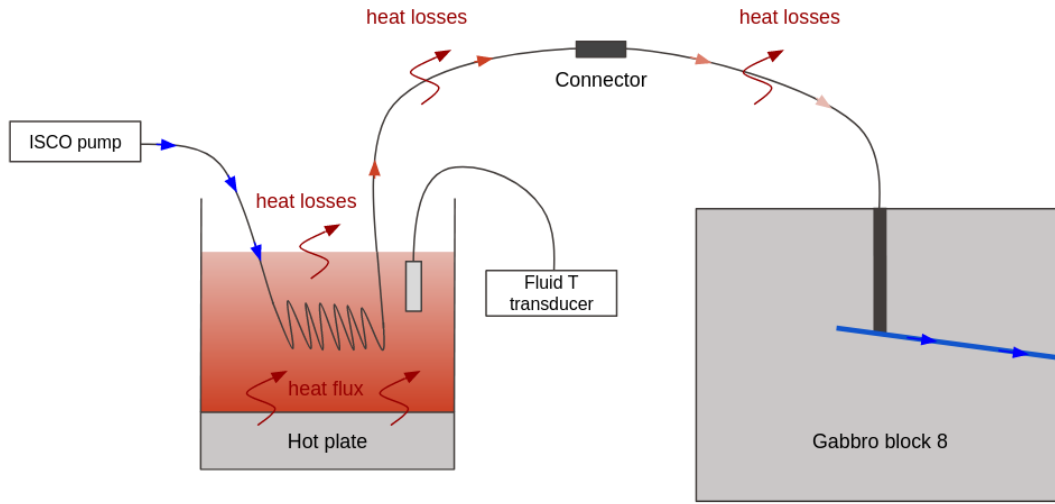


Figure 4.12: Initial FTES experiment setup

To investigate the influence of fluid flow rate on water temperature within the tubing, the connector was opened, allowing for the measurement of water temperature at the midpoint of the tubing using a temperature sensor (Figure 4.13). Then, the silicone oil temperature was set to 130°C , and various flow rates were imposed by the pump. The stabilized temperature was recorded for each rate.

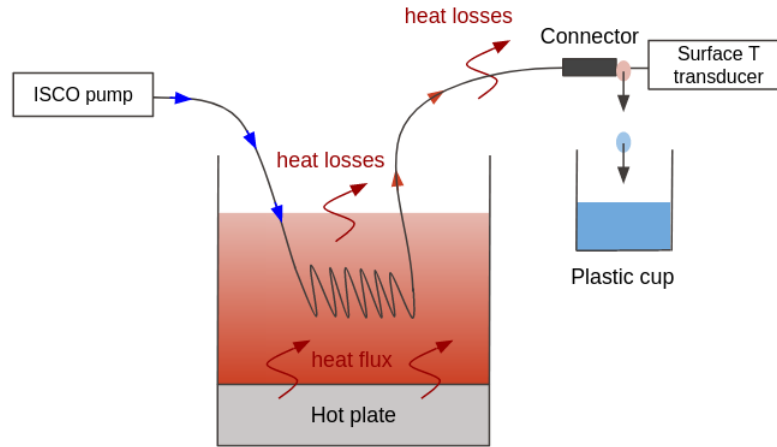
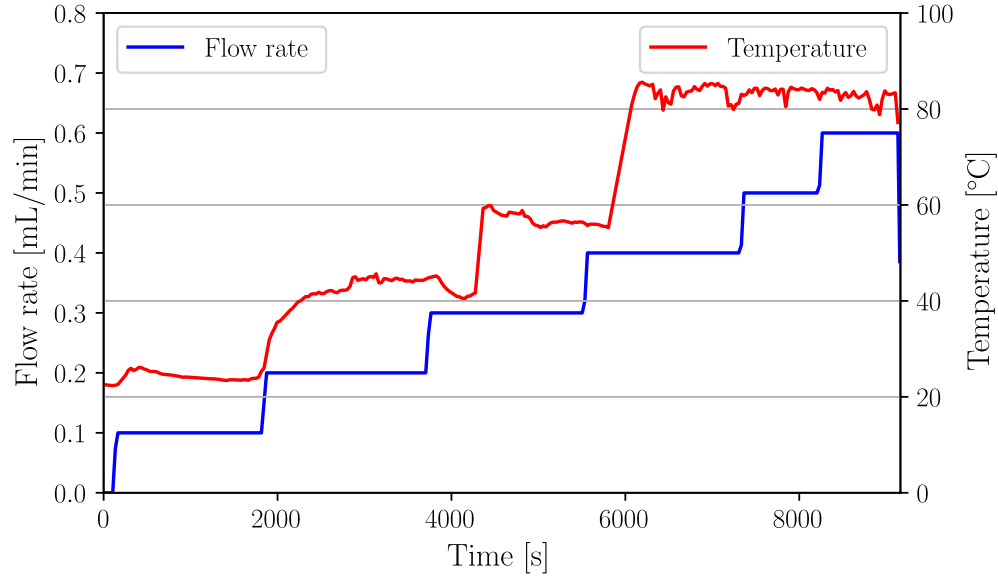


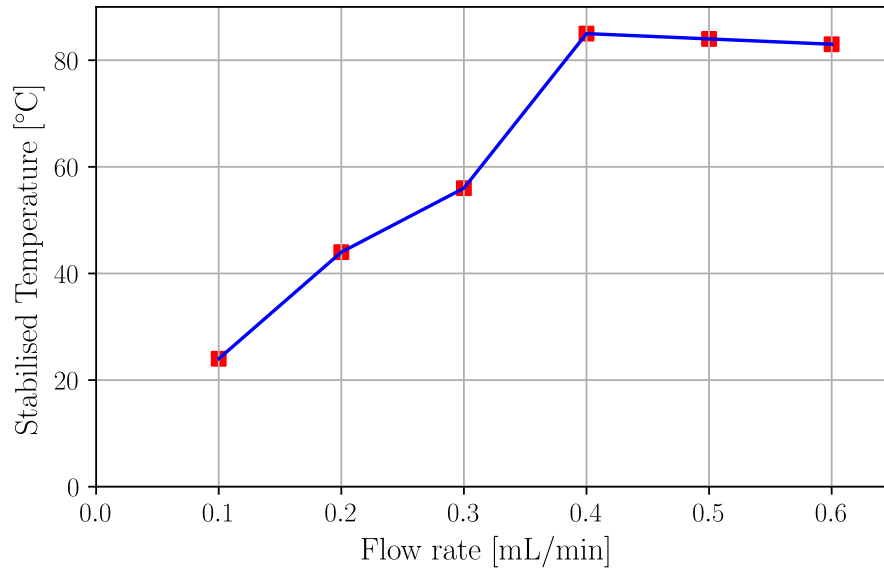
Figure 4.13: Experimental setup for water temperature measurement at the connector

The results of the experiment are shown in Figure 4.14 and demonstrate the existence of two main operating regimes of the system. For flow rates below 0.4 mL/min , the speed of the water is likely slow enough to ensure that the temperature of the water within the heater is equal to that of the silicone oil. However, heat loss along the tubing increases as the water velocity decreases. For flow

rates above 0.4 mL/min, the water entering the heater flows too quickly to reach an equilibrium temperature with the silicone oil. Therefore, the optimal operating flow rate is approximately 0.4 mL/min.



(a) Recorded temperature variation with the temperature sensor for different imposed flow rates



(b) Stabilized temperature for different imposed flow rates

Figure 4.14: Evolution of water temperature at the connector for various flow rates (silicone oil temperature $T_{oil} = 130^{\circ}\text{C}$)

The objective is to determine the water temperature at the inlet of the block rather than at the

midpoint of the tubing. To achieve this, a simplified mathematical model was developed to approximate the water temperature at the block's inlet based on the midpoint water temperature and the relevant physical and geometric properties of the tubing. The model is very similar to the one developed in section 3.2.1, except that it is simpler since it is designed for a steady state regime.

The principle of the model is as follows: consider a cylindrical channel with hot fluid flowing through it. The inlet fluid is at temperature T_0 , and the outside of the tubing is exposed to the ambient air temperature T_∞ . The system can be modeled as one-dimensional, where the energy balance at steady state, considering a length dx along the tubing, is expressed as follows:

$$W c_w \frac{dT}{dx} = -\dot{Q}_h \quad (71)$$

c_w is the specific heat capacity of the fluid and W is the mass flow rate of the fluid inside the tubing, which is given by:

$$W = Q_w \rho_w \quad (72)$$

with Q_w the volumetric fluid flow rate and ρ_w the fluid density.

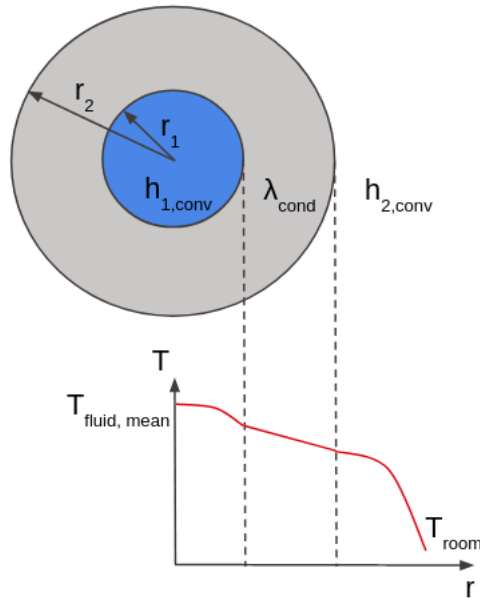


Figure 4.15: Schematic representation of the tubing cross section and corresponding physical properties

Assuming forced convection inside the tubing, conduction through the tubing and natural convection

outside the tubing, the heat transfer rate per unit length of tubing can be written as follows (Spakovszky et al., 2008):

$$\dot{Q}_h = 2\pi r_2 h_0 (T - T_\infty) \quad (73)$$

where h_0 is the overall heat transfer coefficient which is defined as:

$$\frac{1}{h_0} = \frac{r_2}{r_1 h_1} + \frac{r_2}{\lambda} \ln \left(\frac{r_2}{r_1} \right) + \frac{1}{h_2} \quad (74)$$

r_1 and r_2 are respectively the inner and outer radius of the tubing, h_1 is the convective heat transfer coefficient of the fluid inside the tubing, h_2 is the convective heat transfer coefficient of the air outside the tubing, and λ is the thermal conductivity of the tubing.

Rearranging equations 71, 72, 73 gives:

$$\frac{dT}{T - T_\infty} = -\frac{D\pi h_0}{Wc_p} dx \quad (75)$$

where D is the external diameter of the tubing ($D = 2r_2$).

Integrating the previous equation from the beginning of the tubing yields:

$$T(x) = T_\infty + e^{-Ax} (T_0 - T_\infty) \quad (76)$$

where:

$$A = \frac{D\pi h_0}{Wc_p} \quad (77)$$

Based on the continuity of the heat flux, the temperature profile of the outer surface of the tubing can also be determined from the temperature distribution of the fluid along the tubing:

$$T_s(x) = T(x) \left(1 - \frac{h_0}{h'_0} \right) + T_\infty \quad (78)$$

where T_s is the tubing surface temperature, T is the temperature of the fluid found previously and h'_0 is the updated overall heat transfer coefficient that considers only the forced convection inside the tubing and the conduction through it:

$$\frac{1}{h'_0} = \frac{r_2}{r_1 h_1} + \frac{r_2}{\lambda} \ln \left(\frac{r_2}{r_1} \right) \quad (79)$$

The two unknowns of the model are the convective heat transfer coefficients h_1 and h_2 , which can be estimated as follows:

- Convective heat transfer coefficient of the water inside the tubing h_1 .

In general, the convective heat transfer coefficient inside a pipe is computed from the dimensionless Nusselt number Nu , which represents the ratio between convective heat transfer and fluid conduction heat transfer under identical conditions:

$$Nu = \frac{hD}{\lambda} \quad (80)$$

where h and λ are respectively the convective heat transfer coefficient and the thermal conductivity of the fluid inside the tubing.

In the context of the FTES experiment, the internal diameter of the tubing is $\approx 1\text{mm}$, so the ratio λ/D is approximately equal to 600 when considering water. Thus, even considering the worst-case scenario where there is only conduction within water ($Nu = 1$), the heat transfer coefficient is high, and its resistance can therefore be neglected. Consequently, only the unknown h_2 needs to be determined.

- Natural convective heat transfer coefficient of the air close to the tubing h_2 .

The natural convective heat transfer coefficient h_2 is difficult to estimate as it depends on the air flow velocity within the laboratory room and on the geometry, roughness, and temperature of the tubing. However, since the temperature at the connector is known, h_2 can be computed for each fluid flow rate considered during the experiment. The resulting temperature profiles of the fluid along the tubing are shown in Figure 4.16.

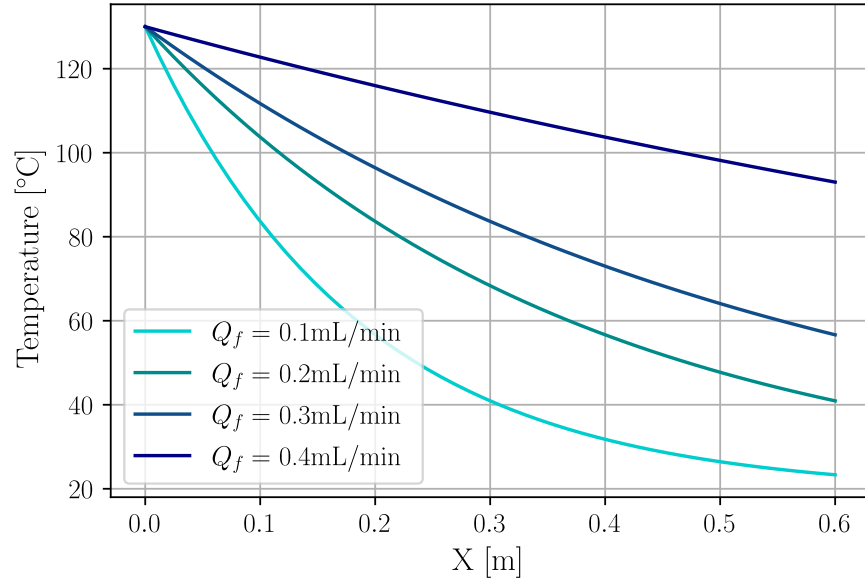


Figure 4.16: Fluid temperature profile along the tubing for various flow rates

As explained in Section 4.2, the flow rate is limited to 0.3 mL/min to prevent the pressures from exceeding 30 MPa. With a fluid flow rate of 0.3 mL/min, the model estimates the temperature of the water at the inlet of the block ($X = 1.1\text{m}$) to be approximately 29°C.

With the current setup, it therefore appears infeasible to inject water at a sufficiently high temperature to heat the block. Two solutions have been proposed to reduce heat loss:

- Shortening the length of the tubing between the heating system and the block.
- Insulating the tubing to minimize heat losses along the tubing.

The new FTES experimental setup is shown in Figure 4.17. The figure is not drawn to scale as the actual length of the pipe has been reduced by a factor of approximately 3.

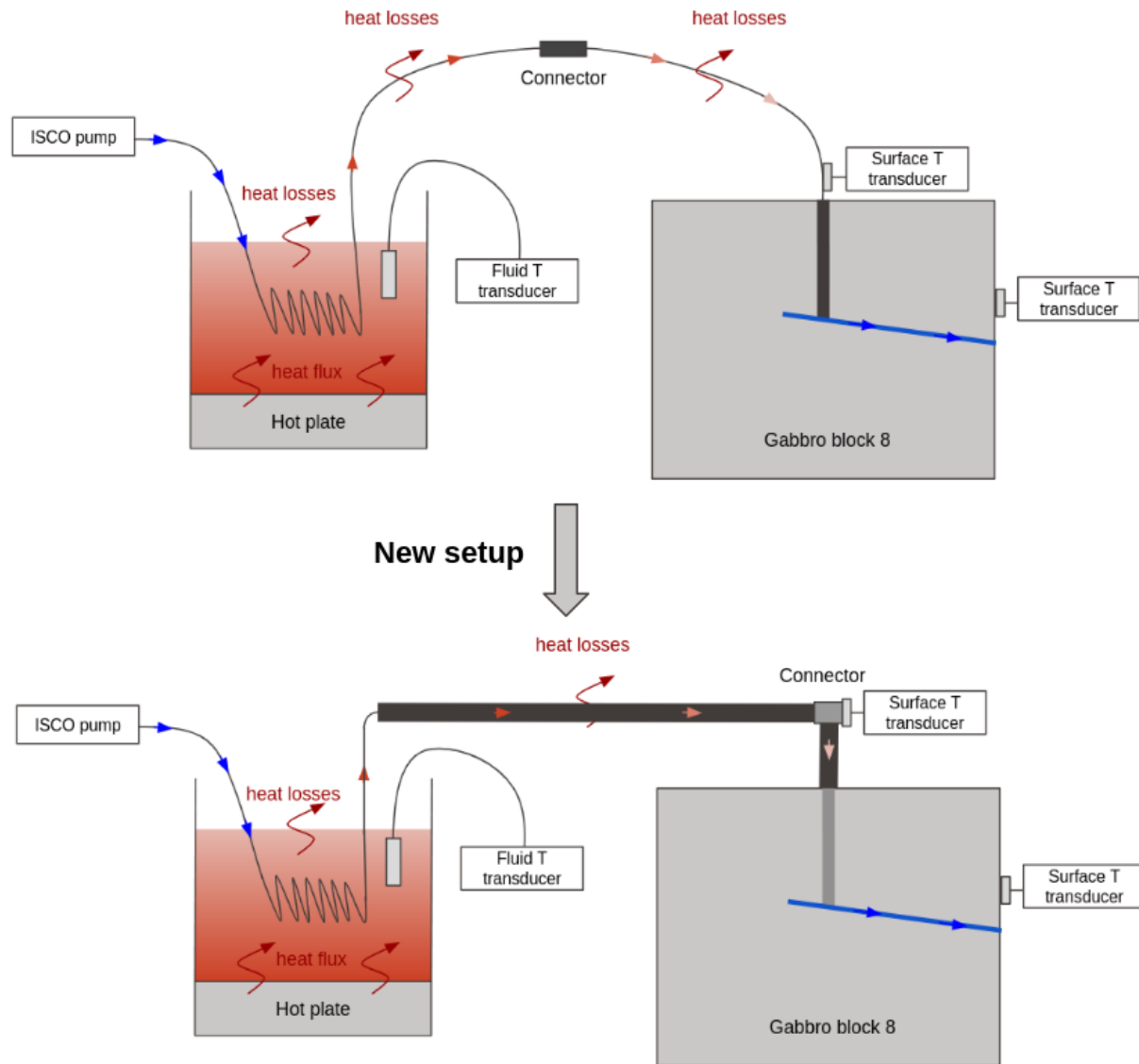
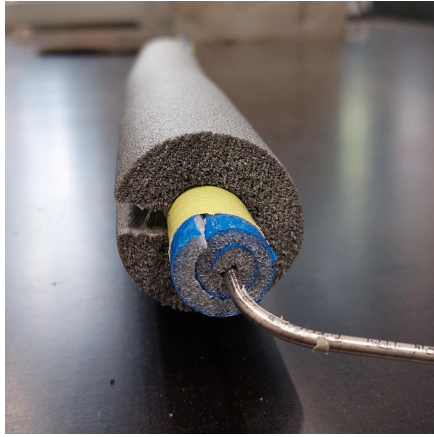


Figure 4.17: Modification of the FTES experimental setup: tubing isolation and shortening



(a) Photograph of the tubing insulation process



(b) Photograph of the resulting insulated tubing

Figure 4.18: Tubing insulation process and result

Following the change of the experiment setup, the experiment to determine the temperature of the water entering the block as a function of the fluid flow rate had to be repeated. The results are shown in Figure 4.19 for different silicone oil temperatures.

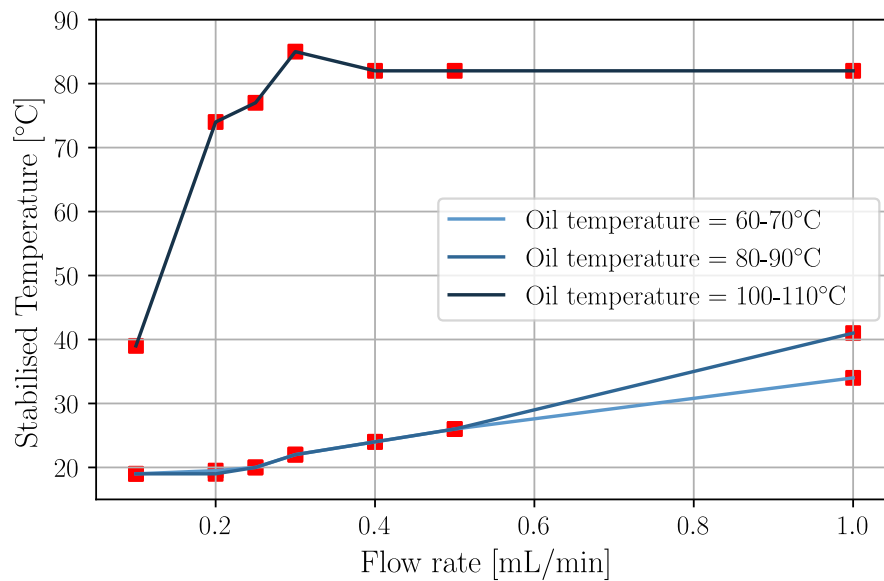


Figure 4.19: Evolution of water temperature at the connector for various flow rates (new experimental setup)

Surprisingly, the Figure 4.19 shows that for oil temperatures below 100 degrees, the temperature of the water at the inlet of the block remains low, even for high fluid flow rates. An explanation for this will be provided in the next section.

4.4.2 Pressurized injection

The experimental setup shown in Figure 4.17 is the final setup developed as part of this project for the laboratory-scale FTES experiment. A first fluid temperature sensor was placed in the beaker to monitor the silicone oil temperature, while two other surface temperature sensors were respectively glued to the tubing near the entrance to the block and to the eastern face of the block, 5 cm above the fracture trace. During the first test of the final experimental setup, the silicone oil was heated to 130 °C. The connector was then closed, and the pump injected at a pressure of 20 MPa to maintain a water flow rate of approximately 0.25 mL/min. The primary objective of this first experiment was to assess whether a small temperature variation would be detectable at the surface of the block after a few hours. To better capture temperature variations on the faces of the block, the entire block was insulated using EPS polystyrene panels, which were glued to each face of the block (Figure 4.20). The temperature surface sensor was glued between the polystyrene panel and the surface of the block. The objective of this insulation was also to ensure near-zero flux boundary conditions at the faces of the block, as assumed in the numerical model presented in Section 3.3.6.

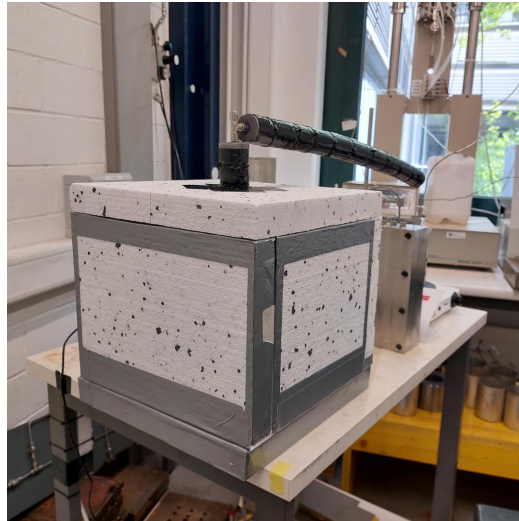


Figure 4.20: Photograph of the insulated gabbro block GB08

However, a few hours after the start of the experiment, the temperature of the tubing at the entrance to the block barely exceeded 23 degrees, and thus the experiment was stopped. To gain insight into this phenomenon, it is essential to understand the changes that occurred when the connector is open compared to when it is closed (i.e., connected to the block):

- In situation 1, where the tubing is not connected to the block, the pressure inside the tubing is close to atmospheric pressure (approximately 100 kPa). When the water in the tubing is heated and the temperature of the silicone oil exceeds 100 °C ($T_{oil} = 130^{\circ}\text{C}$), water vapor is

formed, and these bubbles migrates towards the tubing outlet. The migration of water vapor increases axial convection along the tubing, resulting in enhanced heat transfer. Consequently, the temperature measured at the tube outlet, i.e. at the connector, is elevated (approximately 78°C).

- In situation 2, where the tubing is connected to the block, the pressure inside the tubing is maintained at 20 MPa. This pressure is too elevated to allow water vaporization. Indeed, according to the water phase diagram, water would need to reach approximately 375 degrees to vaporize at 20 MPa. Therefore, convection within the tube is largely reduced as it now depends solely on fluid movement, and the temperature of the water at the connector is significantly lower (approximately 23°C).

This hypothesis is supported by experimental observations, which indicate the presence of condensed water vapor at the connector when the temperature of the silicone oil exceeds 100°C.

In summary, the heating system designed within the scope of this project cannot be used. Indeed, the only way to increase the water temperature, given the current constraints, is to significantly increase the water flow rate. However, this approach is not feasible without reaching considerable pressures that would damage the block. Therefore, a proposition for a new heating system is presented in the following section.

4.5 Discussion

To successfully conduct the laboratory-scale experiment, it appears necessary to change the current heating system, which has the following limitations:

- Excessive heat loss along the tube.
- Limited control over the temperature of the silicone oil, which fluctuates slightly during the experiment due to the operating mode of the hot plate.
- Insufficient feedback on the temperature of the water inside the tubing.
- Safety risks due to the elevated temperature of the silicone oil contained within the beaker.

The suggested new heating system addresses all these limitations by eliminating the need for the hot plate and the beaker filled with silicone oil, and instead heating the water using an electric resistance heating ribbon wrapped around the tubing. This heating ribbon should be connected to a controller that adjusts its power according to the desired water temperature. The current connector configuration already includes a T-shaped connection, which facilitates the introduction

of a fluid temperature sensor at the third branch of the T which is currently sealed. However, this fluid temperature sensor should be thin enough to fit into a 1/8-inch diameter tubing and resistant to pressures up to 25-30 MPa. Finally, the sensor should transmit information about the fluid temperature to the controller, so that it can adjust the power of the ribbon accordingly.

During the numerical modeling of the FTES experiment (Section 3.3), it was demonstrated that a significant temperature variation should be observable on the faces of the block after 2-3 days, depending on the quality of the block's insulation. However, the analysis also revealed that when injecting the water with a flow rate of 0.25 mL/min, the block primarily heats up from the well rather than from the fracture. Consequently, to ensure the modeled system accurately represents an FTES system, the transmissibility of the fracture should also be enhanced so that higher water injection rates can be injected by the pump. This could be achieved by either refracturing the block with confinement to rupture any remaining bridges within the fracture and extend the main fracture towards the west, or by fracturing a new block to establish a more expansive and permeable fracture. The use of a new block would help reduce the wellbore skin effect caused by epoxy fracturing during the creation of the main fracture.

5 Conclusion

The objective of this project was to design a laboratory-scale experiment to investigate the thermal performance of FTES (Fractures Thermal Energy Storage) systems. Initially, the problem was approached from a modeling perspective to gain insights into the two heat transfer processes occurring within an FTES system, namely heat transfer from the well and heat transfer from the fractures. Analytical solutions were presented for both heat transfer problems and were compared to a numerical model developed using the finite element software FEniCS. Then, the numerical model was used to simulate the laboratory-scale FTES experiment. The model demonstrated that significant temperature variation (greater than 5°C) would take at least two days to be detected on the faces of the block if the fluid is injected into the block at a rate of approximately 0.25 mL/min . Furthermore, such temperature variation could only be achieved if the block is effectively insulated to minimize convective heat loss to the surrounding air. Finally, the numerical model indicated that at such a flow rate, heat transfer primarily occurs from the well rather than from the fracture.

In addition to the numerical model, an initial experimental setup was developed for the laboratory-scale FTES experiment. The primary objective of this setup was to establish a controlled circulation of hot water through a horizontally planar fracture, which was created in a $25\times 25\text{ cm}$ gabbro block using hydraulic fracturing. To achieve this, a custom-designed heating system was utilized to heat the water. The heated water was then injected into the block through a central well intersecting the fracture. In order to determine the appropriate range of water flow rates that could be injected into the block without creating a new fracture, the transmissibility of the existing fracture was investigated. The results of the transmissibility tests showed that the maximum allowable operating flow rate is approximately 0.3 mL/min . A water heating system was then designed to directly heat the water inside the tubing. In this system, the tubing was coiled and immersed in a bath of silicone oil heated by a hot plate. However, this heating system was proved to be inadequate in delivering sufficiently hot water at the block's inlet due to significant heat losses along the tubing.

For further development of the laboratory-scale FTES experiment, the following two main aspects should be addressed:

1. Enhancing fracture transmissibility of the GB08 gabbro block:

In order to accurately model the operation of an FTES system, heat transfer must primarily occur from the fracture. Therefore, the injected flow rate by the pump should be increased so that all the energy transported by the water is not dissipated along the well. Moreover, the numerical model demonstrated that doubling the water flow rate injected by the pump (from 0.25 to 0.5 mL/min) would be sufficient to reduce the duration of the experiment from

several days to a single day. The simplest way to enhance fracture transmissibility would be to re-fracture the block with confinement. This would eliminate any remaining bridges within the fracture and extend the main fracture to the west direction. Alternatively, the option of fracturing a new gabbro block could be considered. This approach would overcome any wellbore skin effects caused by epoxy resin infiltration into the fracture, which may potentially reduce the transmissibility of the system.

2. Modifying the heating system:

To reduce heat losses along the tubing, the development of a new water heating system is needed. One possible approach would be to use an electric resistance heating ribbon wrapped around the tubing. By implementing a controller managing the heat flux transmitted from the resistance to the tubing, the temperature of the water entering the block could be precisely regulated. Additionally, this modification would reduce safety risks and automate the heating process.

By addressing the challenges identified and following the proposed recommendations, a more representative and efficient experimental setup for the FTES laboratory-scale experiment should be achieved. The anticipated outcomes derived from this laboratory-scale experiment are expected to significantly enhance our comprehension of FTES systems, fostering advancements in their commercialization and paving the way for their widespread adoption.

References

- Bloemendal, M., Olsthoorn, T., and van de Ven, F. (2015). Combining climatic and geo-hydrological preconditions as a method to determine world potential for aquifer thermal energy storage. *Science of The Total Environment*, 538:621–633.
- Chen, X., Zhao, J., and Chen, L. (2014). Experimental and numerical investigation of preferential flow in fractured network with clogging process. *Mathematical Problems in Engineering*, 2014:1–13.
- Eliasson, T., Sundquist, U., and Wallroth, T. (1988). *Stimulation experiments with water and viscous fluid at the HDR geothermal research site in the Bohus granite, SW Sweden*.
- Geuzaine, C. and Remacle, J.-F. (2009). Gmsh: a three-dimensional finite element mesh generator with built-in pre-and post-processing facilities. *International Journal for Numerical Methods in Engineering*, 79(11):1309–1331.
- Hagoort, J. (2004). Ramey’s wellbore heat transmission revisited. *SPE journal*, 9(04):465–474.
- Hasan, A. and Kabir, C. (1991). Heat transfer during two-phase flow in wellbores; part i—formation temperature. In *SPE Annual Technical Conference and Exhibition*. OnePetro.
- Hellström, G. and Larson, S. (2001). Seasonal thermal energy storage—the hydrock concept. *Bulletin of Engineering Geology and the Environment*, 60:145–156.
- Hesselbrandt, M. and Acuna, J. (2022). Modeling and performance evaluation of fractured thermal energy storage (ftes).
- Janiszewski, M. (2019). *Techno-economic aspects of seasonal underground storage of solar thermal energy in hard crystalline rocks*. PhD thesis.
- Larson, S., Fridh, B., and Haag, Ö. (1983). Hydrock-värmelager i berg. anläggning av värmeväxlarator med hjälp av hydraulisk uppspräckning; hydrock-metoden. Technical report, Technical Report Publ. B 222, Chalmers University of Technology/University of Göteborg.
- Larson, S. Å. (1984). Hydraulic fracturing in the bohus granite, sw-sweden,. test for heat storage and heat extraction. *Geothermal Resources Council TRANSACTIONS*, 8(Aug. 1984):447–449.
- Liu, D. and Lecampion, B. (2022). Laboratory Investigation of Hydraulic Fracture Growth in Zimbabwe Gabbro. *Journal of Geophysical Research (Solid Earth)*, 127(11):e2022JB025678.

- Ramey Jr, H. J. (1962). Wellbore heat transmission. *Journal of petroleum Technology*, 14(04):427–435.
- Ramstad, R. K. (2004). Ground source energy in crystalline bedrock-increased energy extraction by using hydraulic fracturing in boreholes.
- Ramstad, R. K., Hilmo, B., Brattli, B., and Skarphagen, H. (2007). Ground source energy in crystalline bedrock-increased energy extraction using hydraulic fracturing in boreholes. *Bulletin of Engineering Geology and the Environment*, 66:493–503.
- Renshaw, C. E. (1995). On the relationship between mechanical and hydraulic apertures in rough-walled fractures. *Journal of Geophysical Research: Solid Earth*, 100(B12):24629–24636.
- Scroggs, M. W., Dokken, J. S., Richardson, C. N., and Wells, G. N. (2022). Construction of arbitrary order finite element degree-of-freedom maps on polygonal and polyhedral cell meshes. *ACM Transactions on Mathematical Software*.
- Spakovszky, Z. S., Greitzer, M., and Waitz, I. (2008). Thermodynamics and propulsion. *web. mit.edu/16.unified/www/SPRING/propulsion/notes/notes.html*.
- Sundquist, U., Wallroth, T., and Eliasson, T. (1988). *The Fjallbacka HDR geothermal energy research project: reservoir characterisation and injection well stimulation*. Publ. / HDR Geothermal Energy Project, Department of Geology, Chalmers University of Technology and University of Göteborg. Geothermal Energy Project, Department of Geology, Chalmers University of Technology.
- Yeo, I. and Ge, S. (2005). Applicable range of the reynolds equation for fluid flow in a rock fracture. *Geosciences Journal*, 9:347–352.
- Zimmerman, R. W. and Bodvarsson, G. S. (1996). Hydraulic conductivity of rock fractures. *Transport in Porous Media*, 23:1–30.